AGU PUBLICATIONS

JGR

Journal of Geophysical Research: Atmospheres

RESEARCH ARTICLE
10.1002/2017JD027440

This article is a companion to Fritts et al. (2017) https://doi.org/10.1002/2017JD027442.

Key Points:
- Gravity waves exhibit complex dynamics in mesospheric inversion layers
- Responses include trapping, suppressed transmission, reflection, and enhanced shears, instabilities, and dissipation
- MIL penetration is enhanced for larger vertical wavelengths and lower intrinsic frequencies; larger GW amplitudes enable instabilities

Correspondence to:
D. C. Fritts,
dave@gats-inc.com

Citation:
Fritts, D. C., Laughman, B., Wang, L., Lund, T. S., & Collins, R. L. (2018). Gravity wave dynamics in a mesospheric inversion layer: 1. Reflection, trapping, and instability dynamics. *Journal of Geophysical Research: Atmospheres*, *123*, 626–648. https://doi.org/10.1002/2017JD027440

Received 12 JUL 2017
Accepted 15 SEP 2017
Accepted article online 18 NOV 2017
Published online 17 JAN 2018

Gravity Wave Dynamics in a Mesospheric Inversion Layer: 1. Reflection, Trapping, and Instability Dynamics

David C. Fritts[1], Brian Laughman[1], Ling Wang[1], Thomas S. Lund[2], and Richard L. Collins[3]

[1]GATS Inc., Boulder, CO, USA, [2]Colorado Research Associates Division, NorthWest Research Associates, Boulder, CO, USA, [3]Geophysical Institute, University of Alaska Fairbanks, Fairbanks, AK, USA

Abstract An anelastic numerical model is employed to explore the dynamics of gravity waves (GWs) encountering a mesosphere inversion layer (MIL) having a moderate static stability enhancement and a layer of weaker static stability above. Instabilities occur within the MIL when the GW amplitude approaches that required for GW breaking due to compression of the vertical wavelength accompanying the increasing static stability. Thus, MILs can cause large-amplitude GWs to yield instabilities and turbulence below the altitude where they would otherwise arise. Smaller-amplitude GWs encountering a MIL do not lead to instability and turbulence but do exhibit partial reflection and transmission, and the transmission is a smaller fraction of the incident GW when instabilities and turbulence arise within the MIL. Additionally, greater GW transmission occurs for weaker MILs and for GWs having larger vertical wavelengths relative to the MIL depth and for lower GW intrinsic frequencies. These results imply similar dynamics for inversions due to other sources, including the tropopause inversion layer, the high stability capping the polar summer mesopause, and lower frequency GWs or tides having sufficient amplitudes to yield significant variations in stability at large and small vertical scales. MILs also imply much stronger reflections and less coherent GW propagation in environments having significant fine structure in the stability and velocity fields than in environments that are smoothly varying.

1. Introduction

Atmospheric gravity waves (GWs) arise from primary sources such as convection, orography, jets, and frontal systems due to weather in the troposphere and lower stratosphere. GWs are also generated by secondary sources such as wave-wave interactions, the nonlinear dynamics of wave breaking and Kelvin-Helmholtz instabilities (KHI), and body forces due to GW momentum transport extending into the mesosphere and lower thermosphere (MLT). These various sources yield a spectrum of GWs that are ubiquitous throughout the atmosphere and which, together with the instability and turbulence events they spawn, account for much of the multiscale dynamics and the large-scale forcing from the stable boundary layer into the MLT. A broad literature spanning ~6 decades has addressed GW source, propagation, and instability dynamics; the character of the GW spectrum and its variations with altitude; and GW influences on the large-scale circulation and structure throughout the atmosphere. More recent reviews of these various dynamics include Fritts and Alexander (2003), Kim et al. (2003), Plougonven and Zhang (2014), Yiğit and Medvedev (2015), Fritts, Wang, Baumgarten, et al. (2017), and several books, e.g., Sutherland (2010), and Nappo (2013).

The topics of interest in this paper are the GW dynamics that contribute to, and arise in response to, layering in the wind and temperature fields from the surface into the MLT. Temperature structures referred to as "mesosphere inversion layers" (MILs) are suggested to arise due to various dynamics that include the following, to be discussed in greater detail below:

1. planetary wave (PW) breaking, GW breaking and turbulent mixing, and/or GW-tidal interactions that focus GW breaking at slowly descending altitudes (e.g., France et al., 2015; Meriwether & Gerrard, 2004; Whiteway et al., 1995. Salby et al., 2002);
2. climatological inversions capping the tropopause and the polar summer mesopause (e.g., Bell & Geller, 2008; Birner, 2006; Birner et al., 2002; von Zahn & Meyer, 1989);
3. responses to GWs that attain large amplitudes and cause strong wind shears and large variations in local static stability, as often seen in temperature and wind profiles in the stratosphere and MLT (e.g., Liu & Meriwether, 2004; Szewczyk et al., 2013); and

4. multiscale dynamics that yield "sheet and layer" (S&L) structures, arise readily due to wave-wave and wave/mean-flow interactions, instabilities, and turbulence accompanying superposed GWs, and are observed from the surface into the MLT (e.g., Balsley et al., 2003, 2013; Dalaudier et al., 1994; Fritts et al., 2013; Luce et al., 1999).

MILs are frequent, often persistent, features in mesospheric temperature profiles that have been observed in both single-site measurements (Hauchecorne et al., 1987; Schmidlin, 1976) and satellite studies (Clancy et al., 1994). MILs are defined as a layer of increasing temperature in the mesosphere and represent a departure from the expected positive atmospheric lapse rate ($\Gamma = -\partial T/\partial z$) between the stratopause and mesopause. These layers can be ~2–10 km in depth below a local temperature maximum exceeding the background profile mean by ~20–50 K or more. Observations and modeling at global and regional scales reveal that MILs accompany PW breaking below a zero wind line in the PW surf zone, where the PW exhibits an abrupt phase change in the vertical (e.g., France et al., 2015; Gan, Zhang, & Yi, 2012; Irving et al., 2014; Meriwether & Gerrard, 2004; Oberheide et al., 2006; Salby et al., 2002; Sassi et al., 2002; Wu, 2000). These large-scale MILs typically have horizontal scales of several thousand kilometers or more and little or no vertical motion. Large-scale MILs can also exhibit the gradual descent (typically ~1 km/h) of tidal phases due to tidal or large-scale, low-frequency GW modulation of the large-scale wind and temperature fields that are expected to contribute to GW filtering, instability dynamics, local transport, and mixing (e.g., Dao et al., 1995; Liu & Hagan, 1998; Liu & Meriwether, 2004; Meriwether et al., 1998).

Both lidar and satellite measurements have revealed an annual variation in MIL amplitudes, characteristics, and statistics, with maxima in winter at high latitudes and midlatitudes and a semiannual variation at lower latitudes having maxima ~1 month after each equinox (e.g., Cutler et al., 2001; Fechine et al., 2008; Irving et al., 2014; Kumar et al., 2001; Leblanc et al., 1995; Leblanc & Hauchecorne, 1997; Meriwether & Gerrard, 2004).

High-resolution observations by lidars have also revealed the presence of persistent, nearly adiabatic lapse rates on the topside of MILs (Whiteway et al., 1995). These authors used a one-dimensional model to argue that these observations were consistent with the presence of a well-mixed turbulent layer. Wintertime soundings of the mesosphere with Rayleigh lidar and VHF radar showed that MILs coincided with enhanced radar scattering, suggesting that they also coincided with instabilities and turbulence (Thomas et al., 1996). Thomas and coworkers showed the occurrence of radar echoes on both the topside and bottomside of MILs.

Ionization gauge and lidar measurements have often revealed enhanced turbulence in layers with near-adiabatic and superadiabatic lapse rates in the upper mesosphere (Collins et al., 2011; Lehmacher et al., 2006, 2011; Lehmacher & Lübken, 1995; Szewczyk et al., 2013). MILs having smaller horizontal scales have been suggested to be caused by GW breaking and turbulent mixing and heating (e.g., Collins et al., 2011; Duck et al., 2001; Hauchecorne et al., 1987; Whiteway et al., 1995; Williams et al., 2002). These dynamics can also be multiscale in nature, wherein a larger-scale GW or tide provides the background for smaller-scale GWs that might contribute predominantly to instabilities, turbulence, and mixing (Liu & Meriwether, 2004; Szewczyk et al., 2013).

Individual GWs readily attain large amplitudes and cause strong wind shears and large variations in local static stability, as often seen in temperature and wind profiles in the stratosphere and MLT (e.g., Chen et al., 2004; Fritts et al., 2004; Goldberg et al., 2006; Hauchecorne & Chanin, 1980; Keckhut et al., 1990; Meriwether et al., 1994; Tsuda et al., 1991; Wang et al., 2006; Williams et al., 2006). Importantly, events interpreted as MILs include a continuum of dynamics ranging from stable, large-scale features attributed to PW critical levels to local and transient features arising due to multiscale GW and larger-scale flows yielding S&L structures throughout the atmosphere. The latter suggest an inability to distinguish between active GW instability and turbulence events and their implications for the background temperature fields.

Multiscale dynamics that yield S&L structures readily arise due to advection and associated instabilities and turbulence accompanying superposed GWs and larger-scale flows and are observed from the surface into the MLT (e.g., Balsley et al., 2003, 2013, 1998; Chuda et al., 2007; Coulman, 1973; Coulman et al., 1995; Dalaudier et al., 1994; Fritts et al., 2004; Gossard et al., 1985; Luce et al., 1995, 1999; Muschinski & Wode, 1998; Nastrom & Eaton, 2001; Schneider et al., 2015). These dynamics typically have layer scales that vary from ~10 to 200 m in the stable boundary layer, ~20 m to ~1 km in the troposphere and lower stratosphere, ~100 m to ~5 km in the middle and upper stratosphere, and ~1 to 20 km in the MLT. In each

case, highly stratified (large buoyancy frequency, N) and sheared sheets separate layers having much weaker stratification and shear, often with the sheets being ~10 times or more thinner, and having N^2 and local wind shears ~10 times or more larger than mean values (see references above and Fritts et al., 2013, 2016, and Fritts & Wang, 2013). Sheets can also occur at very much smaller scales, e.g., as thin as ~1 m in the stable boundary layer and ~100 m or less in the MLT, with local minima accompanying strong advection by instabilities extending to even smaller scales (Baumgarten et al., 2012; Fritts, Wang, Baumgarten, et al., 2017; Miller et al., 2015).

Studies cited above have revealed significant diversity in the correlations of instabilities and turbulence with the background stability, suggesting equally diverse underlying dynamics. This can be understood to some degree by noting that there are several types of dynamics at play. In relatively simple environments, medium- and high-frequency GWs exhibit breaking where the nondimensional horizontal velocity perturbation, $a = u'/(c - U)$ (with GW horizontal velocity u', phase speed c, and mean wind U in the plane of propagation), approaches or exceeds 1 (Achatz, 2005, 2007; Fritts et al., 2009a, 2009b). This implies one or several near-adiabatic or superadiabatic lapse rates separated by a vertical wavelength that may extend over several kilometers in the vertical. The GW amplitude a will increase because of either (1) u' growth with altitude due to a constant vertical flux of horizontal momentum, $\rho<u'w'>$, where $<>$ denote a spatial or temporal average; (2) approach to a critical level where $c = U$, causing u' to vary as $(c - U)^{-1/2}$ in shear flow for conservative motions; and/or (3) increasing N, which causes increasing $|u'/w'| = |m/k| = |N/k(c - U)|$ for constant k, c, and U (e.g., Fritts & Alexander, 2003) The result is local instabilities leading to turbulence that arise in, and remain closely associated with, the initial nearly adiabatic layer for several buoyancy periods, $T_b = 2\pi/N$ (e.g., Fritts et al., 2009b). What remains unknown at present is whether GW breaking results in significant changes in environmental stability.

The same environmental influences cause low-frequency inertia-GWs (IGWs) to preferentially exhibit KHI whether the shear layer is statically stable or unstable (Lelong & Dunkerton, 1998a, 1998b), especially when the IGW shears enhance local mean shears where the local Richardson number, $Ri = N^2/[(du/dz)^2 + (dv/dz)^2] < 1/4$, for total zonal and meridional winds, u and v. KH billow depths and intensities are functions of Ri and the Reynolds number, $Re = Uh/\nu$, where h is the half depth of the shear layer and ν is the effective viscosity, either the kinematic viscosity, ν, or potentially a turbulent viscosity, ν_{turb}, for which there is recent observational evidence (Fritts et al., 2014; Hecht et al., 2014). Unlike GW breaking, however, there is clear observational and modeling evidence that energetic KHI occurring for small Ri and large Re do yield approximately adiabatic layers following billow mixing and prior to restratification (e.g., Coulman et al., 1995; Fritts et al., 2012; Thorpe, 1973a, 1973b; Werne & Fritts, 1999; Woodman et al., 2007). Hence, it is challenging to determine whether a near-adiabatic layer in an IGW environment is a result of a large-amplitude IGW or due to mixing of a resulting KHI.

Finally, theory predicts that increases in N enhance the tendency for local instabilities and turbulence due to GW breaking and IGW KHI (VanZandt & Fritts, 1989), for the reasons noted above. The most persistent responses are expected in regions of enhanced static stability capping the tropopause and the polar summer mesopause, and radar, balloon, aircraft, and rocket measurements appear to confirm these expectations (e.g., Lübken, 1997; Lübken et al., 2002; Nastrom & Eaton, 2001; Rapp et al., 2004; Whiteway et al., 2003). Such enhanced instabilities and turbulence also have significant impacts on the vertical propagation of GWs through these regions (e.g., Gisinger et al., 2017).

Summarizing the more idealized mechanisms driving instabilities and turbulence, (1) GW breaking exhibits strong correlations of turbulence with weak or negative static stability within the GW field, but not because of mixing; (2) KHI due to large-amplitude IGWs yields strong mixing and slow restratification for sufficiently small Ri and large Re, with turbulence highly correlated with weak stratification prior to restratification; and (3) GW breaking induced in regions of large N leads to correlations that are opposite to those seen in active GW breaking.

In more complex multiscale environments, which often occur at all altitudes below the turbopause, superposed GWs and mean flows yield local KHI events and GW breaking that differ in important respects from their simpler forms in more idealized flows. Larger-scale KHI always occurs on the sheets of enhanced temperature and velocity gradients, in the absence of IGWs in many cases, because the spatial and temporal evolutions of these sheets driven by the multiscale GW field often yield $Ri < 1/4$ due to enhanced shears or sheet

thinning (Fritts et al., 2013, 2016). Smaller-scale KHI on the sheets also often occur accompanying strong upward displacements due to GW breaking, as seen in observations and numerical studies (e.g., Baumgarten & Fritts, 2014; Fritts et al., 2013). GW breaking yields plunging that occurs primarily in the deeper layers between sheets, but which also entrain the leading KHI at small scales. Other instabilities that arise in multiscale flows are intrusions comprising thin, rapid tongues of air most often moving in the direction of primary GW propagation. These were first identified in numerical simulations (e.g., Fritts et al., 2013; Fritts & Wang, 2013) and subsequently recognized in images of small-scale dynamics revealed in polar mesospheric clouds (Fritts, Wang, Baumgarten, et al., 2017; Miller et al., 2015). Like GWs, intrusions appear to trigger small-scale KHI induced by strong shears at their upper and lower edges as they evolve toward thinner configurations.

The consequences of instability and turbulent mixing events are of significant interest throughout the atmosphere. At present, however, there is little observational guidance on mixing efficiency for known turbulence sources, except for KHI events that occur at large scales and have long durations, such that standard instruments (e.g., radars, lidars, balloons, and aircraft) have been able to perform detailed studies (e.g., Blumen et al., 2001; Fukao et al., 2011; Gossard et al., 1985; Luce et al., 2002). These have revealed both stronger events (inferred $Ri \sim 0.05–0.15$) that drive the temperature toward an adiabatic gradient between sheets of high shear and stratification and weaker and shallower events (inferred $Ri \sim 0.2$) that do not result in separate sheared and stratified sheets. Modeling of KHI in both idealized and multiscale environments has confirmed the strong dependence of mixing efficiency on the initial Ri (and Reynolds number, Re) (e.g., Fritts et al., 2012, 2016; Werne & Fritts, 1999). However, three-dimensional (3-D) modeling of GW breaking events that have addressed turbulence and mixing dynamics have not been performed. Hence, estimates of mixing efficiency to date have relied on theoretical efforts, inferences from parameterizations in global models, and two-dimensional (2-D) modeling that also requires assumptions (e.g., Chao & Schoeberl, 1984; Coy & Fritts, 1988; Dunkerton & Fritts, 1984; Fritts & Dunkerton, 1985; Hauchecorne et al., 1987; Liu & Hagan, 1998; Liu et al., 2000; Liu & Meriwether, 2004; McIntyre, 1989; Schoeberl et al., 1983; Strobel et al., 1987, 1985; Walterscheid & Schubert, 1990). Importantly, none of these estimates have been confirmed, and the consequences for mixing accompanying GW dynamics are likely to be highly diverse, given the strong dependence of GW instability processes on environmental conditions.

Our focus in this study is on the dynamics accompanying an upward propagating GW packet encountering representative stronger and weaker MILs (or no MIL) for several GW packet characteristics. The model and its configuration for our purposes are described in section 2. Model results comparing GW responses for the various MIL and GW cases are described in section 3. Section 4 discusses our results in the context of various observations. A summary and our conclusions are provided in section 5.

2. Anelastic Model and Simulation Parameters

2.1. Anelastic Model

The model employed for this study was described in detail by Lund and Fritts (Lund & Fritts, 2012, hereafter LF12). It employs the finite-volume (FV) architecture discussed by Felten and Lund (2006) to discretize the anelastic Navier-Stokes equations, yielding an anelastic FV model that results in exact numerical conservation of mass, momentum, and kinetic and thermal energy (apart from explicit dissipation) and thus faithfully represents the underlying conservation laws. A consequence of energy conservation is that the scheme has no numerical dissipation. The anelastic formulation enables descriptions of GW and instability dynamics extending to high altitudes, as needed for various applications. Additional details on the model formulation and equations can be found in LF12 and Bannon (1996).

The FV model employs periodic boundary conditions in the horizontal, a flat or variable free-slip or no-slip lower boundary, and a radiation condition and/or a sponge layer to avoid GW reflection at the upper and lower boundaries. It supports either idealized or realistic wind and stability environments that can evolve in time from specified initial fields (e.g., mean and tidal fields) in response to GW and turbulence momentum and heat transport and turbulent heating. GW excitation can occur at the lower boundary, as a specified initial packet in one, two, or three dimensions (1-D, 2-D, or 3-D), in response to imposed heat or momentum sources, or in superposition as needed. Instabilities and turbulence that arise due to increasing GW amplitudes can be described either via direct numerical simulation (DNS) that resolves the 3-D turbulence

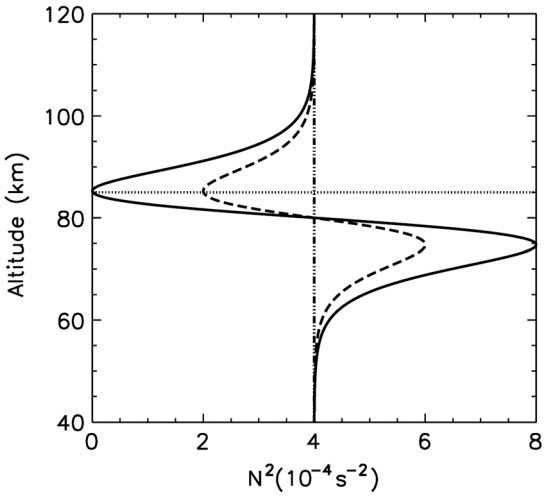

Figure 1. N^2(z) profiles for the MIL simulations: no MIL, b = 0 (dash-dotted); weak MIL, b = 0.5 (dashed); and strong MIL b = 1 (solid). The horizontal dashed line at 85 km highlights where N^2(z) = 0 for reference in subsequent figures.

spectrum for sufficiently high model resolution and low Reynolds numbers, $Re = c\lambda_z/\nu = \lambda_z{}^2/\nu T_b$ (where $\nu = \mu/\rho$, ρ, and T_b are kinematic viscosity, density, and buoyancy period), or via a dynamic large-eddy simulation method described by Germano et al. (1991).

2.2. Simulation Parameters and GW Packet Specification

We assume an environment with a background isothermal atmosphere below the MIL with $T(z)$ = 240 K, such that the density scale height is H = 7 km, with mean density $\rho(z) = \rho_0 e^{-z/H}$, mean buoyancy frequency squared $N_0{}^2 = 4 \times 10^{-4}$ s^{-2}, and mean buoyancy period $T_b = 2\pi/N$ = 314 s. The MIL structure imposes local and higher-altitude departures from an isothermal atmosphere and is specified such that $N^2(z) = N_0{}^2$ {1 − βC tanh[$(z - z_M)/h$] sech^2[$(z - z_M)/h$]}, where $C = 3^{3/2}/2$ allows $N^2(z)$ to vary from 0 to $2N_0{}^2$ for β = 1, z_M = 80 km is the altitude of transition from enhanced to decreased $N^2(z)$, and h = 8 km determines the vertical structure of the MIL feature. This yields a separation of the peak and minimum N^2 of z_{MIL} ~ 10 km. We assume β = 0, 0.5, or 1 for our various cases (see profiles in Figure 1). The model domain extends one GW horizontal wavelength in the streamwise (x) direction, 2 km in the spanwise (y) direction (for our 3-D cases), and from −100 to 200 km in altitude, with damping layers in the lower and upper 50 km. This $N^2(z)$ implies $dT/dz > 0$ above ~95 km that is roughly consistent with the observed mesopause.

We assume a GW propagating in the (x,z) plane having perturbations u', w', and T' of initial form $\varphi' = \varphi_0{}'$ exp[$-(z - z_0)^2/2\sigma^2$] exp[$z/2H + i(kx + m_0 z - \omega t)$], where z_0 = −20 km is the altitude of maximum initial GW momentum flux, σ = 20 km, and peak initial amplitudes occur at ~8.55 km. Here $k = 2\pi/\lambda_x$ and $m_0 = 2\pi/\lambda_{z0}$ are the GW horizontal and initial vertical wave numbers, with horizontal and initial vertical wavelengths λ_x and λ_{z0}; $\omega = kc$ is the GW frequency in the domain frame of reference with initial value ω_0. Additionally, c is the GW horizontal phase speed and $\omega_i = k(c\text{-}U)$ is the intrinsic frequency with respect to the mean wind U. For our purposes here, we consider GW λ_x and λ_{z0} varying from 10 to 40 km to span the MIL depth. Several considerations contributed to the chosen GW scales. Initial simulations revealed that significantly smaller λ_{z0} exhibited essentially no transmission, while larger λ_{z0} are not frequently observed at large amplitudes. Likewise, initial simulations demonstrated that increasing λ_x for fixed λ_{z0} systematically increases MIL transmission; hence, other cases at larger λ_x would add few additional insights to those described below.

The anelastic Navier-Stokes equations yield a GW dispersion relation in a nonrotating, isothermal atmosphere that agrees closely (for vanishing ν and thermal diffusivity) with the GW branch of the inviscid compressible acoustic-GW dispersion relation (Bannon, 1996). For reference, this dispersion relation may be written as

$$m^2 = k^2\left(N^2/\omega_i{}^2 - 1\right) - 1/4H^2 \quad (1)$$

Here N is the atmospheric buoyancy frequency and k, m, and ω_i are as defined above.

In order to achieve solutions relevant to the MLT at manageable spatial resolution, we assume a turbulent viscosity, $\nu_{turb} = 30\nu$, where $\nu \sim 1.5 \times 10^{-5}$ m^2 s^{-1} is the true kinematic viscosity at the Earth's surface. There are at least three justifications for this assumption. First, many in situ measurements reveal mean turbulence energy dissipation rates of $\varepsilon \sim 10^{-3}$ W kg^{-1} W kg^{-1} or larger at altitudes above ~70 km in summer and winter (Lübken, 1997; Lübken et al., 2002; Rapp et al., 2004; Szewczyk et al., 2013). These are typically ~1 decades larger than $\varepsilon_{min} \sim \nu N^2$ and imply significant background turbulence intensities. Second, combined observational and modeling studies of secondary instabilities accompanying KHI seen in OH airglow and noctilucent clouds have revealed much larger secondary instability scales than are predicted for Re based on kinematic viscosity, implying turbulent viscosities $\nu_{turb} \sim 5$–40ν at these altitudes (Fritts et al., 2014; Hecht et al., 2014). Finally, high-resolution imaging of polar mesospheric clouds at ~82 km reveals frequent evidence of large-scale instabilities and/or turbulence implying a turbulence "inner scale" $l_0 \sim 10(\nu^3/\varepsilon)^{1/4}$ often as small as ~10–20 m and $\varepsilon \sim 0.01$–1 W kg^{-1} (Fritts, Wang, Baumgarten, et al., 2017; Miller et al., 2015). The inner scales implied by ν_{turb}=30ν and the peak horizontally-averaged ε~0.4 m^{2}s^{-3} for the 3-D simulations

Table 1
GW Parameters for Each Case Performed

Case	λ_x (km)	λ_{z0} (km)	T_{GW} (s)	ω_0 (N)	c (m s^{-1})	u_0' (m/s)	b	Lin/NL	2-D/3-D	Δx, Δy, Δz (m)
1a	20	20	450	0.7	44.4	0.00062	0	Lin	2-D	50/–/50
1b	20	20	450	0.7	44.4	0.00062	0.5	Lin	2-D	50/–/50
1c	20	20	450	0.7	44.4	0.00062	1	Lin	2-D	50/–/50
2a	20	20	450	0.7	44.4	0.062	0	NL	2-D	50/–/50
2b	20	20	450	0.7	44.4	0.062	1	NL	2-D	50/–/50
2c	20	20	450	0.7	44.4	0.062	1	NL	3-D	20/20/20
3a	20	40	417	0.75	55.8	0.00082	1	Lin	2-D	50/–/50
3b	20	40	417	0.75	55.8	0.082	1	NL	2-D	50/–/50
3c	20	40	417	0.75	55.8	0.082	1	NL	3-D	20/20/23.5
4a	10	10	445	0.7	22.4	0.00039	1	Lin	2-D	50/–/50
4b	10	10	445	0.7	22.4	0.039	1	NL	2-D	50/–/50
5a	20	10	493	0.64	28.3	0.00031	1	Lin	2-D	50/–/50
5b	20	10	493	0.64	28.3	0.031	1	NL	2-D	50/–/50
6a	40	20	509	0.62	55.8	0.00076	1	Lin	2-D	50/–/50
6b	40	20	509	0.62	55.8	0.076	1	NL	2-D	50/−/50

described here are l_0~135 and 86 m, respectively (see the companion paper by Fritts et al., 2017b). Hence, we employ a spatial resolution for the 3-D simulations of ~20 m, which is marginally sufficient to describe the inertial range without reliance on the dynamic LES.

In general, nonzero kinematic (or turbulent) viscosity and thermal diffusivity will alter the dispersion and polarization relations increasingly with altitude, but these have small influences for the GW scales and altitudes considered here. Additional model details are provided by Lund and Fritts\ (2012).

Finally, we will employ wave action density, defined as $A = E/\omega_i$ (where E is total GW energy density), the integral over the GW packet of which is constant for conservative GW propagation in variable environments, to show the spatial and temporal evolutions of the GW fields in the various cases examined.

3. FV Simulations of GW-MIL Encounters

GWs are assumed to have λ_x and initial λ_{z0} of 10, 20, or 40 km, λ_{z0}/λ_x varying from 0.5 to 2, corresponding initial ω_0 from ~N/2.24 to N/1.2. The corresponding temporal variation of GW amplitude at a fixed altitude for each packet prior to interactions with the MIL is approximately Gaussian with a standard deviation, $\tau \sim \sigma_0/c_{gz}$, where c_{gz} is the GW vertical group velocity. The GW and model parameters for each case are listed in Table 1.

3.1. Linear Reflection and Transmission for $\lambda_x = \lambda_{z0} = 20$ km and $\beta = 0$, 0.5, and 1

We begin by examining the relative evolutions of a GW packet having $\lambda_x = \lambda_{z0} = 20$ km and a very small amplitude encountering a weaker and stronger MIL and without a MIL present. These three cases (Cases 1a–1c in Table 1) are compared showing temporal evolutions of streamwise-vertical (hereafter streamwise) cross sections of u' for $\beta = 0$, 0.5, and 1 from 10 to 27 T_b in Figure 2. For these and later cases, the u' (x,z) fields are shown in a reference frame moving with the initial GW c (to the left) thus having $U(z,t = 0) = -c > 0$ (to the right) in this frame. The u' cross sections for this and all cases discussed below have color scales chosen to display the peak amplitudes and thus vary widely. The u' fields are thus not representative of the GW kinetic energy density due to the varying color scales and decreasing density with altitude.

Without the MIL (Figure 2, Case 1a, $\beta = 0$), the GW u' grows exponentially in amplitude, approximately preserves its form despite strongly increasing amplitude, and penetrates to higher altitudes where it is dissipated rapidly above ~120 km, rather than ~150 km, due to the assumed enhanced turbulent viscosity. The weaker MIL and associated lower stability above (Figure 2, Case 1b, $\beta = 0.5$) causes significant reflection and reduction (by ~60%) of the transmitted GW A, e.g., see the $A(z)$ profile at 20 T_b (green line) in subpanel b of Figure 2 at lower right. The stronger MIL (Figure 2, Case 1c, $\beta = 1$) causes effective trapping and nearly complete reflection of the GW in the MIL between ~67 and 85 km. See, e.g., the layering that reveals superposed upward and downward propagating GWs in the MIL at 15 and 17 T_b and largely downward GW radiation thereafter. The

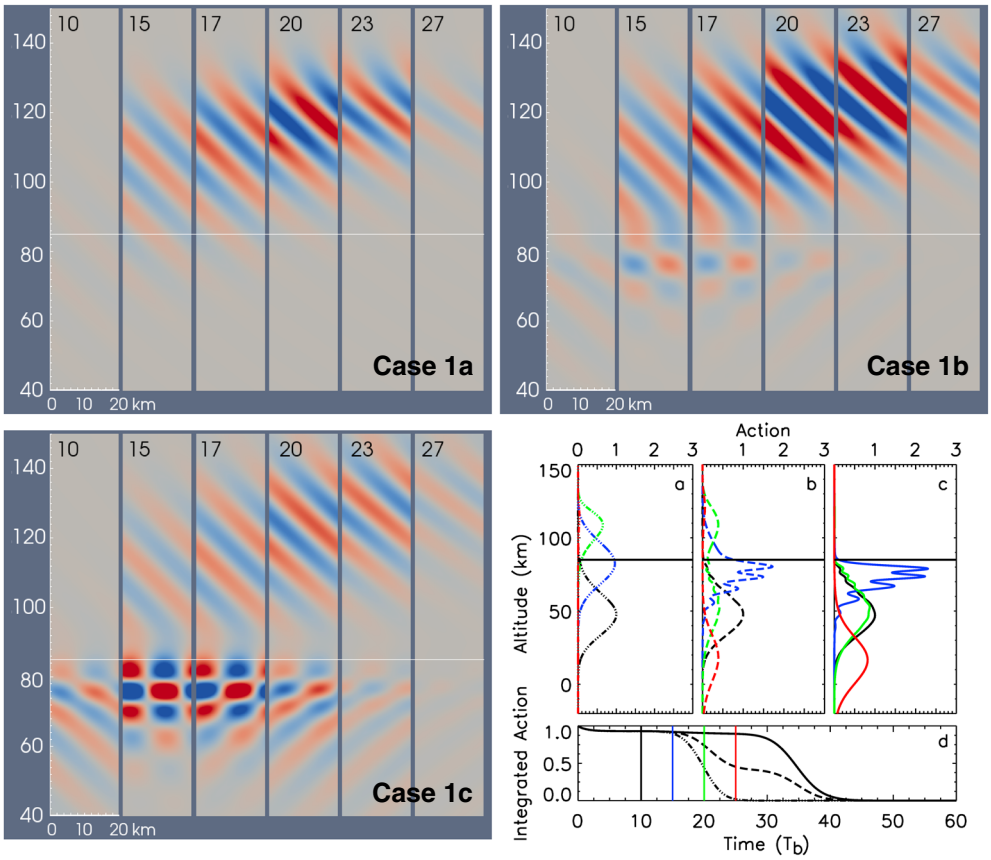

Figure 2. Cases 1a–1c streamwise u' cross sections for $b = 0$, 0.5, and 1, respectively, at the times shown in T_b (left to right in each panel). Contour limits are ±2, 0.7, and 0.2 m s^{-1} for Cases 1a–1c, respectively. Profiles at lower right are GW action density $A(z)$ for Cases 1a–1c (subpanels a–c) and integrated $A(t)$ (subpanel d). Line types are dash-dotted, dashed, and solid for Cases 1a–1c, respectively; the line colors in the $A(z)$ profiles correspond to the times indicated by these colors in subpanel d.

comparable amplitudes of the transmitted GW at 100 km and the reflected GW at 60 km imply a peak transmitted $A \sim 0.003$ in Case 1c.

The incident, transmitted, and reflected GW wave action density, A, normalized to $A = 1$ at the peak at initiation is shown as vertical profiles at intervals of 5 T_b for the three cases and integrated over the entire domain, respectively, in subpanels a–d in Figure 2 at lower right. $A(z)$ is computed assuming no GW self-acceleration in the induced mean jets, given their shallow extent, and the challenges of assessing $\omega_i = k(c\text{-}U)$ in a narrow portion of a strongly nonlinear response. This likely leads to a small overestimate of A due to a local underestimate of ω_i in the jet.

The integrated A evolutions for the three cases (see subpanel d of Figure 2 at lower right) between ~15 and 40 T_b confirm rapid dissipation at higher altitudes without the MIL, the ~50% transmission and delayed dissipation of the GW A in Case 1b, and the nearly complete reflection and persistent trapping in Case 1c. The initial ~5% reduction of integrated A in each case results from the initial GW packet having a tail extending into the lower model sponge layer, and it occurs for all of the cases considered here.

3.2. Nonlinear Responses for $\lambda_x = \lambda_{z0} = 20$ km and $\beta = 0$ and 1

The linear results discussed above suggest intensification of the GW response in a MIL relative to that without a MIL due to GW reflection, as seen in Figure 2, Case 1c and lower right. Hence, we anticipate that a GW encountering a MIL with sufficient amplitude may lead to nonlinear dynamics and potential instability due to the MIL at a lower amplitude (and altitude) than would occur without the MIL. Cases 2a–2c describe the corresponding responses for GWs that are 100 times larger in amplitude than Cases 1a–c. Case 2a

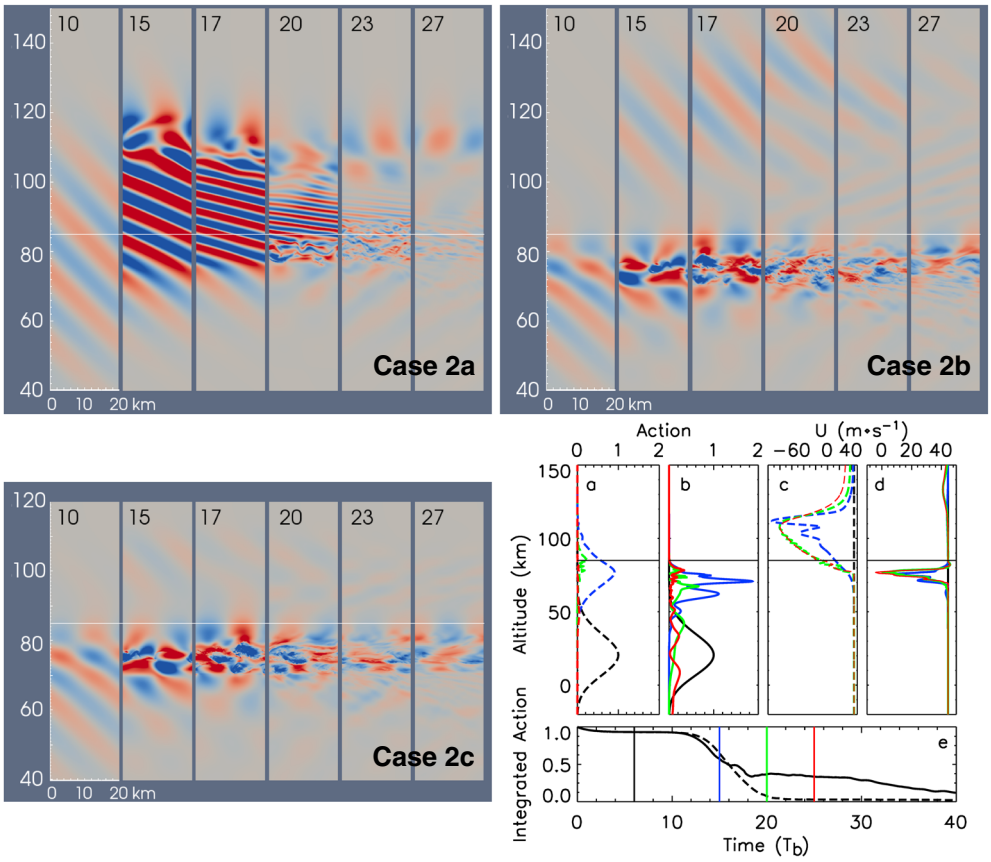

Figure 3. As in Figure 2 but for nonlinear responses with contour limits of ±20 m s^{-1}. Case 2a is for $b = 0$, and Cases 2b and 2c for $b = 1$ are 2-D and 3-D simulations, respectively. At lower right, subpanels a and b show $A(z)$, subpanels c and d show $U(z)$ due to momentum flux divergence, and subpanel e shows $A(t)$ (dashed and solid) for Cases 2a and 2b, respectively. The line colors are as in Figure 2.

addresses a large-amplitude GW without a MIL that is stable at the MIL altitude, but which exhibits "self-acceleration" (SA) instability dynamics at higher altitudes (e.g., Fritts et al., 2015). Case 2b addresses the same GW for a MIL with $\beta = 1$ performed in 2-D, and the MIL in this case induces GW trapping and a smaller λ_z by ~1.7 times at the peak $N^2 = 2\ N_0{}^2$ (see equation (1)), hence intensified shears, instabilities, and dissipation within the MIL. Because Case 2b exhibits instabilities, Case 2c examines these dynamics in 3-D in order to resolve the 3-D instability and turbulence dynamics and evaluate the validity of the 2-D results. The *Re* ~40,000 for $\lambda_z = 20$ km is sufficiently large for the assumed ν_{turb} ~40 $m^2\ s^{-1}$ at ~80 km to allow vigorous instabilities and turbulence (e.g., Fritts et al., 2009b).

Streamwise cross sections of u' for Cases 2a–2c are shown in Figure 3 at the same times displayed in Figure 2 (10–27 T_b). Comparing Cases 2a–2c with Cases 1a and 1c in Figure 2 reveals several major differences. Without a MIL, the Case 2a GW exhibits 2-D SA instability beginning just before 15 T_b near and below ~120 km, as noted above. The presence of a MIL in Cases 2b and 2c prevents these SA dynamics by largely trapping the GW in the MIL. As in Case 1c, trapping is initially driven by refraction of the GW to a smaller λ_z within the MIL and strong reflection of the GW at the region of low N^2 above the MIL. The large GW amplitude in Cases 2b and 2c has three effects not occurring in Case 1c. First, the large GW amplitude implies a large momentum flux, $\rho < u'w' > (z)$, only a small fraction of which is transmitted through the MIL. Second, the large GW amplitude in the MIL induces instabilities leading to turbulence. And third, trapping and dissipation of the GW in the MIL implies flow accelerations accompanying flux divergence, i.e., $dU(z)/dt = -(1/\rho)\ d[\rho < u'w' > (z)]/dz$. The second of these, GW dissipation accompanying instabilities and turbulence, begins at ~15 T_b and results in much reduced transmitted and reflected GWs at later times (compare the u' cross sections and A profiles for Cases 1c, 2b, and 2c in Figures 2 and 3).

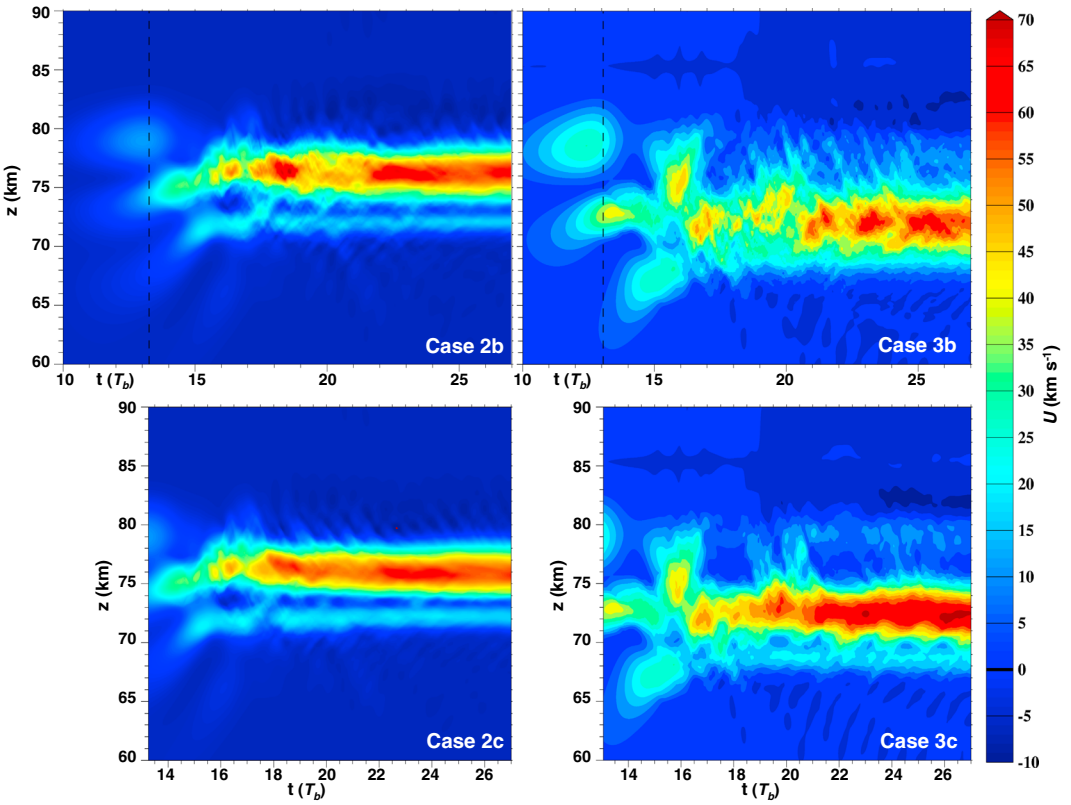

Figure 4. $U(z,t)$ changes in the direction of GW propagation for Cases 2b and 2c (top and bottom left plots) and Cases 3b and 3c (top and bottom right plots) from 10 to 27 T_b due to GW momentum flux divergence accompanying GW instabilities and dissipation in the MIL. The 3-D fields at bottom were initiated at 13.3 and 13.1 T_b prior to initial instabilities.

Profiles of $U(z)$ and contours of $U(z,t)$ showing the effects of momentum flux divergence in Case 2b (see subpanels b and d of Figure 3 at lower right) and for Cases 2b and 2c (Figure 4, left column) reveal that these dynamics occur rapidly (spanning ~3 T_b) and establish a stable $U(z)$ jet in the MIL along the GW c having a peak magnitude of ~60 m s^{-1} that is ~30% larger than the initial GW phase speed that persists after GW dissipation.

The evolving mean winds, $U(z,t)$, for Cases 2b and 2c shown at left in Figure 4 reveal a number of interesting and surprising features. There is a close correspondence between the 2-D and 3-D evolutions at larger scales, despite the inability of the 2-D simulation to describe the 3-D instabilities that lead to turbulence and mixing (see below). Indeed, this is consistent with the close agreement seen between the two u' field evolutions for Cases 2b and 2c in Figure 3.

Each case exhibits a weaker, narrower $U(z)$ maximum at ~72 km and a stronger, wider $U(z)$ maximum centered at ~76 km (i.e., ~1–2 km above the maximum N^2 and having a full width at half maximum (FWHM) of ~2.5 km. Inspection of Figure 3 (Cases 2b and 2c at 17 T_b) and Figure 4 (left column) reveals that the larger $U(z)$ maximum corresponds closely to the altitude showing the strongest initial instability dynamics in the evolving GW field in the MIL. We also note stronger small-scale structure in the 2-D $U(z)$ and u' fields at later stages, which is likely due to the more efficient (and physical) dissipation accompanying real 3-D instabilities and turbulence in Case 2c.

Both evolutions exhibit transient features that comprise ascending and descending $U(z,t)$ variations beginning ~16 T_b extending above the MIL, and to a lesser degree below, that decay as the instabilities and turbulence subside. Inspection of the $U(z,t)$ fields at left in Figure 4 and the u' (x,z) fields at specific times at left in Figure 5 reveals these to be due to transient GW features with varying phase slopes (hence momentum transport), caused by temporal evolutions of the larger-scale instabilities within the GW and instability fields. Near

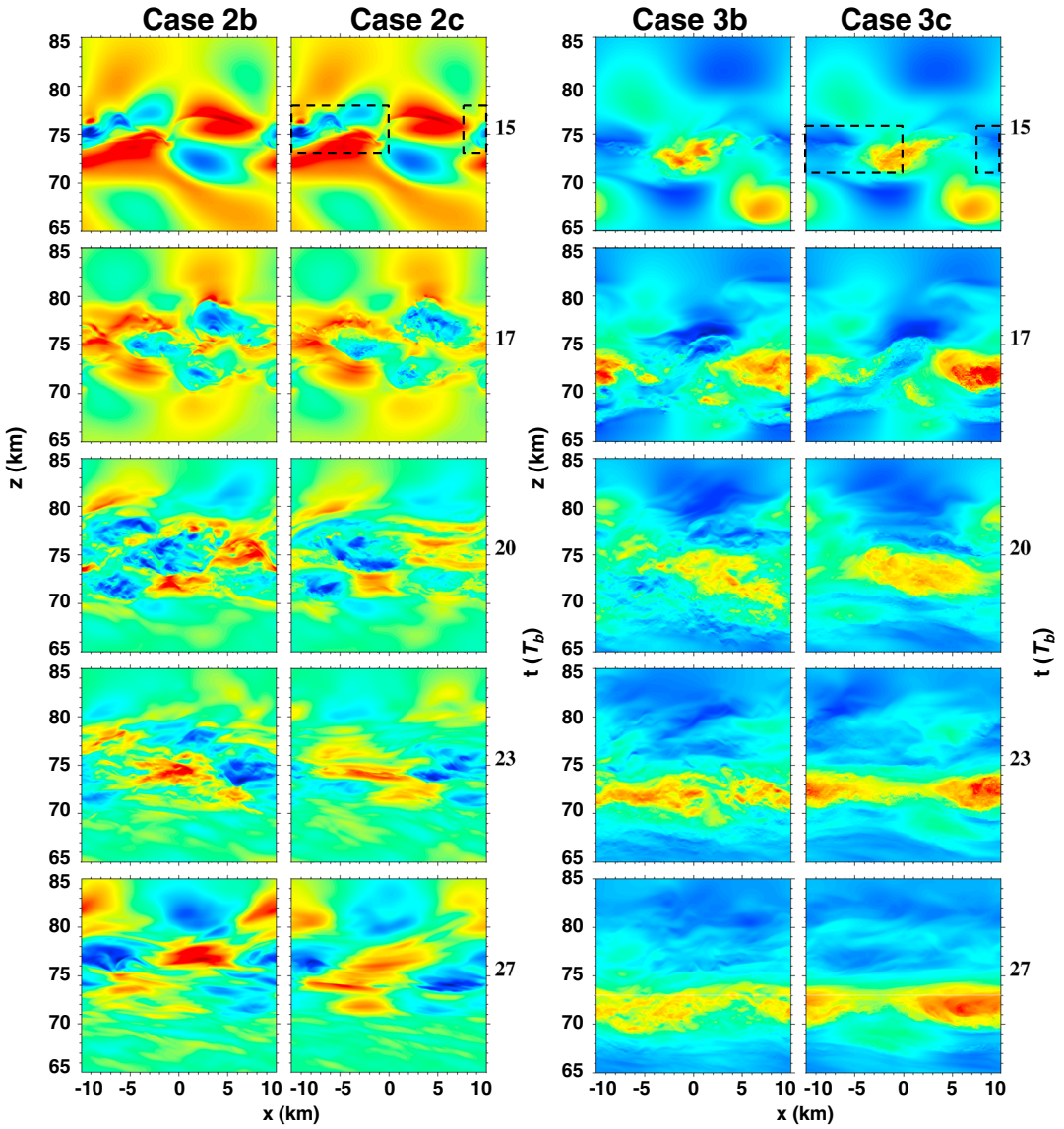

Figure 5. Streamwise u' cross sections highlighting the small-scale instability and turbulence dynamics from 65 to 85 km for Cases 2b and 2c (left and middle left plots) and Cases 3b and 3c (middle right and right plots) at 15, 17, 20, 23, and 27 T_b (top to bottom). The colors in each case vary from blue (negative) to red (positive) with ranges that decrease with GW amplitudes. The dashed rectangles at top for Cases 2c and 3c show initial instabilities in regions exhibiting GW overturning ($N^2 < 0$) ~2 T_b earlier.

the $U(z,t)$ maxima, these transient GWs have propagating behavior in the vertical (e.g., small $c - U$, large N^2, and hence real $m = 2\pi/\lambda_z$ from equation (1). But as they propagate outward from the MIL, increasing $c - U$ and decreasing N^2, hence imaginary m implying evanescence, cause their reflection and a reversal of the vertical momentum transport. These features decay more rapidly with time in Case 2c, due to the more rapid and realistic dissipation enabled by resolved 3-D instabilities and turbulence.

Additional evidence of this variability is seen in the $A(z)$ and $U(z)$ profiles in subpanels b and d in Figure 3 at lower right. Both the $A(z)$ and $U(z)$ profiles exhibit significant spatial structure on small vertical scales within the MIL at these times. In each case, these altitudes are where we might expect turning levels based on increasing $c - U$ and decreasing N^2. Importantly, this behavior is distinct from the initial GW transmission and reflection occurring prior to trapping of the GW, its forcing of the strong $U(z)$ profile, and the variations of the GW phase structure within the MIL accompanying this "self acceleration." $A(z)$ profiles are not shown

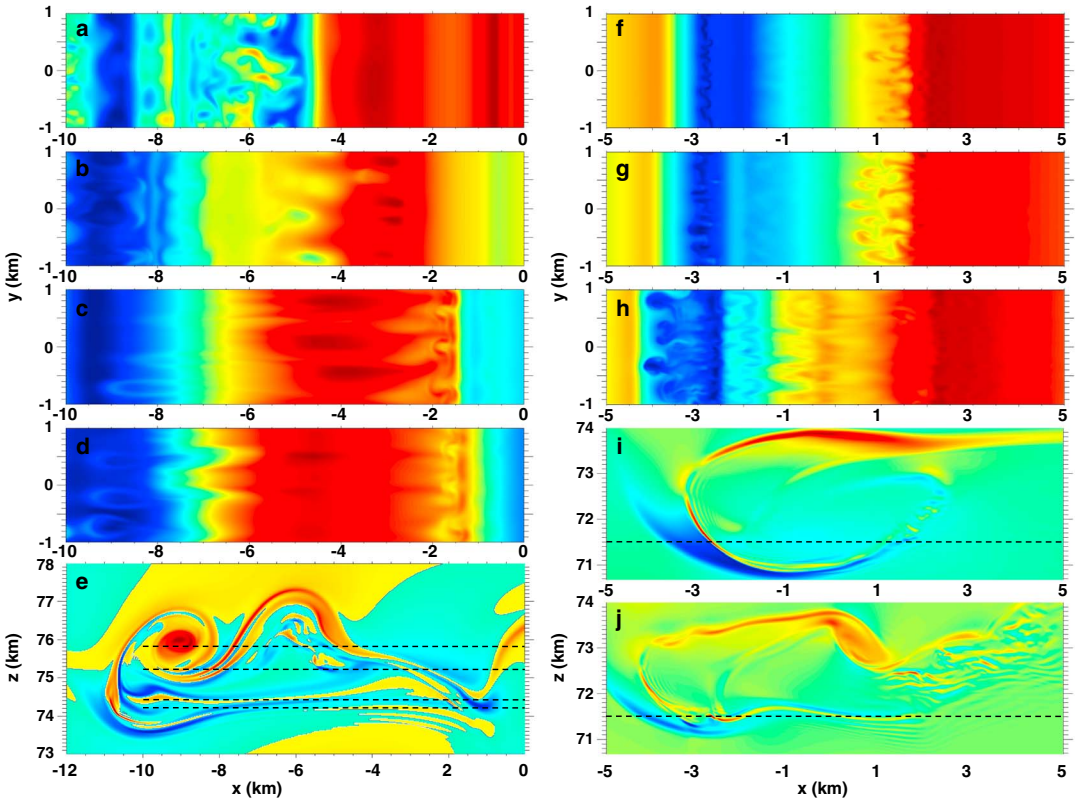

Figure 6. (a–d) Case 2c u' (x,y) at 15 T_b and z = 75.8, 75.2, 74.4, and 74.2 km and (e) spanwise vorticity, $\zeta_y(x,z)$, showing the structures of initial small-scale instabilities. The locations of the Case 2c u' cross sections are shown with dashed lines in Figure 6e; the location of the ζ_y cross section is shown with a dashed rectangle in the cross section at top, middle left (at 15 T_b) in Figure 5. (f–h) Case 3c u' (x,y) at 15 T_b and 71.5 km at 13.5, 13.6, and 13.8 T_b and (i and j) streamwise vorticity, $\zeta_y(x,z)$, at 13.5 and 13.8 T_b. The location of the Case 3c u' cross sections is shown with dashed lines in Figures 6i and 6j.

for Case 2c, as they differ only slightly from those for Case 2b until after ~20 T_b, where $A(z)$ is already small. As in Case 1c, integrated $A(t)$ persists to late times in Cases 2b and 2c due to GW trapping, despite reductions due to dissipation in the MIL.

Finally, it is intriguing that the large-amplitude 2-D and 3-D cases with the MIL yield apparently similar GW phase structures, $U(z,t)$ evolutions, GW dissipation, and even transient momentum transports at the edges of the induced mean jet. This is despite the inability of Case 2b to properly account for the 3-D transition to turbulence and GW dissipation. To explore this in greater detail, we compare the transitions to smaller scales in the u' (x,z) fields spanning the instability evolutions over 12 T_b for Cases 2b and 2c at left in Figure 5 (times of 15, 17, 20, 23, and 27 T_b). At the earliest time shown (~1.7 T_b after initiation of the 3-D Case 2c), the two fields exhibit initial instability dynamics that have only begun to diverge due to 3-D structures in Case 2c. The 2-D u' fields remain nearly identical at 17 T_b and reveal increasing differences at 20 T_b and thereafter. In each case, however, the major differences occur at the smallest spatial scales. The larger-scale features remain similar, with the largest differences being the weaker u' magnitudes and increased layering in Case 2c at the latest times. This suggests that 3-D turbulence in Case 2c is more effective at dissipating GW energy than the artificial constrained 2-D dynamics in Case 2b. Turbulence kinetic energy evolutions will be discussed below.

Throughout these evolutions, and despite their differing GW amplitudes and dissipation, the larger-scale spatial structures comprising the remaining ducted GW responses in the MIL for Cases 2b and 2c have maintained their relative phase structures. They also exhibit similar phase slopes, but varying in time, above and below the MIL at these different times, confirming the role of GW transience in vertical momentum transport observed in Figure 4 and discussed above.

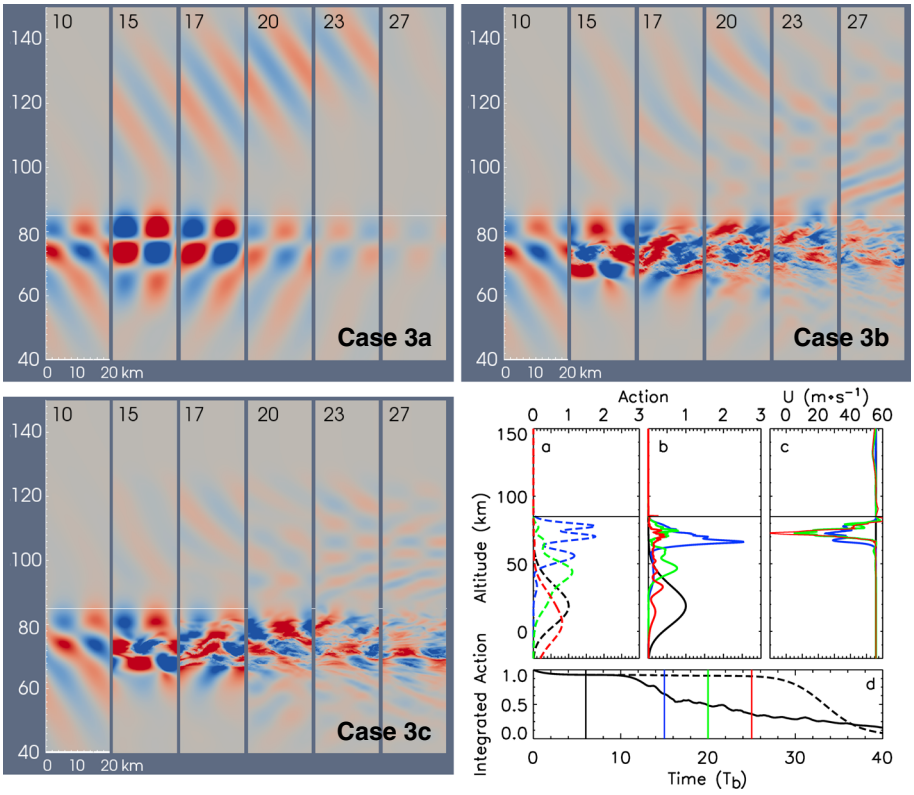

Figure 7. As in Figure 3 for Cases 3a–c for $b = 1$. Case 3a is linear; Cases 3b and 3c are nonlinear and 2-D and 3-D, respectively. Contour limits are ±0.2 and 20 m s^{-1}, respectively, for Case 3a and Cases 3b and 3c. Subpanels at lower right show $A(t)$ for Cases 3a and 3b, $U(z)$ for Case 3b, and integrated $A(t)$ for Cases 3a and 3b.

Figures 6a–6d show horizontal cross sections of u' at 15 T_b that reveal the spanwise character of the initial 3-D instabilities leading to turbulence and GW dissipation in Case 2c. These are at altitudes of the small-scale features at center left in the top plot at 15 T_b of the Case 2c results (see the dashed box in Figure 5 and the dashed lines in Figure 6e). Figures 6c and 6d reveal vortex loops at left arising from streamwise-aligned (spanwise wave number) counterrotating vortices that are advecting to the left (blue). Similar features at comparable scales moving rapidly to the right ($u' > 0$) are seen in the positive phase of the larger-scale structure at right (red). In both regions, the dominant spanwise scale is ~600–700 m. Inspection of a streamwise cross section of spanwise vorticity, $\zeta_y = du'/dz - dw'/dx$, in a small subdomain (Figure 6e), however, reveals that these larger-scale features have opposite rotation in the streamwise plane. The feature at left resembles KHI structure and behavior; that at right has weak and variable, but opposite, larger-scale ζ_y. The horizontal cross sections in Figures 6a and 6b are nearer the cores of these features and reveal that the instabilities in the cores are further advanced than in the external shears at this time. The subsequent evolutions of these features show a rapid transition to smaller-scale turbulence features that are largely confined to the regions of negative large-scale u'.

3.3. Linear and Nonlinear Responses for λ_x = 20 km, λ_{z0} = 40 km, and β = 1

We now examine the responses for linear and nonlinear GWs having $\lambda_x = 20$ km, $\lambda_{z0} = 40$ km, and $\beta = 1$ (Cases 3a–3c, see Table 1). As in Case 2c, we perform a 3-D nonlinear simulation (Case 3c) to evaluate the ability of the 2-D nonlinear simulation (Case 3b) to capture the GW evolution in the presence of strong instability and turbulence dynamics. Streamwise u' cross sections for these cases are shown from 10 to 27 T_b (same times as for Cases 1 and 2) in Figure 7. The linear response (Case 3a) most closely resembles Case 1c. In each, strong trapping (ducting) in the MIL occurs centered from 15 to 17 T_b, though the higher ω_i and c_{gz} in Case 3a cause this response to occur somewhat earlier than in Case 1c. In each, the maximum MIL response is also followed by transmitted and reflected GWs that largely decay by 27 T_b. As in Case 1c, the $A(z)$ profiles in Case 3a reveal

that the transmitted GWs are nearly negligible. The comparable maximum amplitudes of the reflected and transmitted GWs at ~50 and 100 km for Case 3a imply a peak transmitted GW $A \sim 0.001$, thus smaller than for Case 1c due to the higher ω_i in this case.

Both similarities and differences are seen in comparing the u' cross sections for Cases 2b and 2c in Figure 3 with those for Cases 3b and 3c in Figure 7. Similarities include the following:

1. formation of strong layering prior to 15 T_b, as seen in the linear cases, and nearly complete confinement in the MIL thereafter;
2. large GW amplitudes and du'/dz in the MIL that lead to strong deformations and initial 2-D instabilities arising by 15 T_b, and to rapid GW breakdown thereafter; and
3. rapid cessation of transmitted and reflected GWs following initial instabilities.

Differences between the two cases seen in the u' cross sections include the following:

1. larger GW λ_z in the MIL in Cases 3b and 3c, but decreased by a larger fraction than for Cases 2b and 2c at the peak N^2, see equation (1), and
2. a more persistent MIL response at larger vertical scales and extending to lower altitudes in Cases 3b and 3c than in Cases 2b and 2c.

We now compare Cases 3b and 3c to evaluate the importance of resolving 3-D instabilities and turbulence for cases in which these dynamics are stronger than in Cases 2b and 2c. $U(z)$ profiles for Case 3b at 15, 20, and 25 T_b are shown in subpanel c of Figure 7 at lower right. $U(z,t)$ contours from 10 to 27 T_b for Cases 3b and 3c are shown at top and bottom right in Figure 4. The 2-D and 3-D instabilities and turbulence structures are shown with u' cross sections between 65 and 85 km from 15 to 27 T_b at right in Figure 5. The initial instability evolution and scales at the strongest initial vorticity sheet driving instability dynamics are illustrated with u' horizontal cross sections at 71.5 km at 13.5, 13.6, and 13.8 T_b and with streamwise-vertical ζ_y cross sections in a 10 × 3.5 km subset of the horizontal and vertical domain at 13.5 and 13.8 T_b at right in Figure 6.

Assessments of the conditions leading to the initial instabilities in Cases 2b, 2c, 3b, and 3c prior to the u' fields at top in Figure 5 reveal that instabilities are triggered by GW breaking within the MIL in each case. The onset conditions occur ~2 T_b prior to the instabilities seen evolving at top in Figure 5. Importantly, they accompany the earlier, and more coherent, descending and leftward moving regions of negative (blue) u' indicated in the dashed rectangles for Cases 2c and 3c at 15 T_b. In each, the advection by upward and downward propagating GWs in the MIL drives a region of negative N^2 centered in descending regions of negative (blue) u', indicating overturning of the GW fields in the MIL at these earlier times.

As seen in Cases 2b and 2c, the large-scale evolutions of the Case 3b and 3c $U(z)$ fields and profiles are similar in many respects, and similar in their gross features to those in Case 2. Weak initial accelerations arise at multiple altitudes, but coalesce into single major jets centered at ~72.5 km from ~10 to 17 T_b. Notably, the jets are centered ~3.5 km below those in Cases 2b and 2c, and ~2 km below the peak N^2 (see discussion of instability and turbulence fields below). Both 2-D and 3-D cases again exhibit transient momentum transports out from, and back into, the jets on time scales of a few T_b extending to intermediate or late times, but largely above the jets.

Differences in the 2-D and 3-D jet evolutions are greater than seen in Cases 2b and 2c. The contraction of the jet in altitude is slower and does not yield as compact a jet in Case 3b as in Case 3c. The jet in Case 3b is also weaker than in Case 3c throughout the evolutions; i.e., the peak magnitudes are ~55 and ~70 m s^{-1} and their FWHM are ~5 and 3.5 km at later times in Cases 3b and 3c, respectively. These differences are due to the differing influences of 2-D and 3-D descriptions of the GW instability and turbulence fields, which are clearly more significant in Cases 3b and 3c than in Cases 2b and 2c.

GW $A(z)$ profiles for Case 3b (see subpanel b in Figure 7 at lower right) reveal that instabilities act to trap the GW in the MIL and significantly reduce the reflected GW by 15 T_b. Despite strong dissipation, larger $A(z)$ remains in the MIL in Case 3b than in Case 3a at 20 and 25 T_b, though the reflected (or radiated) GW $A(z)$ is much smaller than in Case 3a at these times.

Differences between the nonlinear evolutions in Cases 2 and 3, and between Cases 3b and 3c, are revealed in greater detail in zoomed u' cross sections at altitudes from 65 to 85 km at times from 15 to 27 T_b in Figure 5.

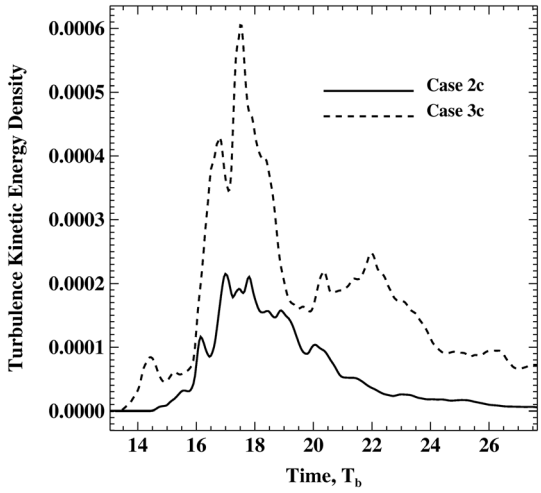

Figure 8. Temporal variations of TKE density (per unit volume) averaged from 60 to 90 km for Cases 2c and 3c (solid and dashed lines, respectively). Note the stronger, more variable, and extended TKE for Case 3c having larger energy inputs.

Comparing first Cases 2 and 3, we note that Cases 3b and 3c exhibit significantly larger-scale GW perturbations in altitude, as implied by the deeper layering within the MIL noted in the discussion of Figure 7. This results in instabilities and turbulence occurring primarily at altitudes of ~68 to 75 km in Cases 3b and 3c, as compared to ~72 to 78 km in Cases 2b and 2c. The different altitude ranges correspond closely to the edges of the induced mean jets in Cases 2 and 3 because permanent mean flow changes can only accompany GW dissipation. Energetic small-scale instabilities and turbulence extend beyond ~20 T_b in all cases, but GW forcing of instabilities and dissipation within the MIL, and their modulation of transient momentum fluxes, remain stronger in Case 3 than in Case 2. This is consistent with the more sustained GW amplitudes and the more variable jet structures at later times in Case 3 (see the GW amplitudes in Figures 3 and 7 and the jet variability in Figure 4). Examining the small-scale flow features in Cases 2 and 3 at later times in Figure 5, it is clear that 3-D turbulence is more efficient in driving energy dissipation in each case and that it subsides more quickly thereafter.

Figures 6f–6h show horizontal cross sections of u' at 13.5, 13.6, and 13.8 T_b at 71.5 km (dashed lines in Figures 6i and 6j) for Case 3c. These instabilities arise at the strongest initial ζ_y sheet driven by the large-amplitude GW within the MIL and occur ~1 T_b earlier than in Case 2c (compare the instabilities in Figure 6 at left for Case 2c at 15 T_b with those at right for Case 3c at 13.5–13.8 T_b). These have initial spanwise scales of ~200–400 m, thus ~2–3 times smaller than in Case 2c; they also evolve and cascade more rapidly to smaller instability scales and turbulence relative to Case 2c. The initial instabilities in both Cases 2c and 3c have the same forms observed to arise at similar unstable ζ_y sheets in DNS of idealized GW breaking, the transition to turbulence in KHI at small *Ri* and large *Re*, and in multiscale flows throughout the atmosphere (Fritts et al., 2009b, 2012, 2013, 2016). As seen in Case 2c, 3-D instabilities and turbulence in Case 3c account for stronger GW dissipation and increasing departures from the 2-D evolution in Case 3b with time. Stronger turbulence and more rapid GW dissipation in Case 3c also yield much less residual GW activity in the MIL at late times (compare the bottom plots of Figure 5).

Turbulence kinetic energy evolutions for Cases 2c and 3c averaged between 60 and 90 km are compared in Figure 8. These reveal quite different temporal evolutions. Case 2c exhibits a single peak near 17–18 T_b having a peak mean turbulence kinetic energy (TKE) density (per unit volume) of ~0.0002 kg m^{-1} s^{-2}. In contrast, Case 3c TKE arises earlier at small amplitude and exhibits a narrow, significant maximum of ~0.0006 kg m^{-1} s^{-2} at ~17.5 T_b and a second, broader maximum from ~20 to 23 T_b. Importantly, the Case 3c TKE maxima are ~3 times the Case 2c maximum at comparable times throughout the simulations.

3.4. Linear and Nonlinear Responses for $\lambda_x = \lambda_{z0} = 10$ km and $\beta = 1$

Cases 4a and 4b (see Table 1) describing MIL responses for linear and nonlinear GWs having $\lambda_x = \lambda_{z0} = 10$ km and $\beta = 1$ are illustrated with streamwise cross sections of u' from 20 to 44 T_b in Figure 9 (top and middle), respectively. Because 2-D and 3-D instability dynamics yielded very similar GW transmission and reflection in the more energetic Cases 2 and 3, we assume that a 2-D description of nonlinear influences is a useful guide for weaker nonlinearities here.

Both Cases 4a and 4b exhibit strong trapping (ducting) that yield nearly complete reflection, thus very weak transmission, but only after long residence times in the MIL. These are similar to the results for Cases 2b and 3b, but occur on longer time scales due to the smaller c_{gz} in this case. The GW responses within the MIL are highly structured in the vertical, due to the small initial λ_{z0} and its compression by ~1.7 times at the peak $N^2 = 2\,N_0^2$, as in Cases 2 and 3. This yields strong shears and instabilities in Case 4b that significantly dissipate the GW before the times at which strong GW reflection is seen in Case 4a (compare Figure 9, top and middle, beginning ~28 T_b). Because of the small λ_x and λ_{z0} and weak transmission (due to large negative m^2 above the MIL), transmitted and/or radiated GWs have almost invisible amplitudes using the same color scale as below

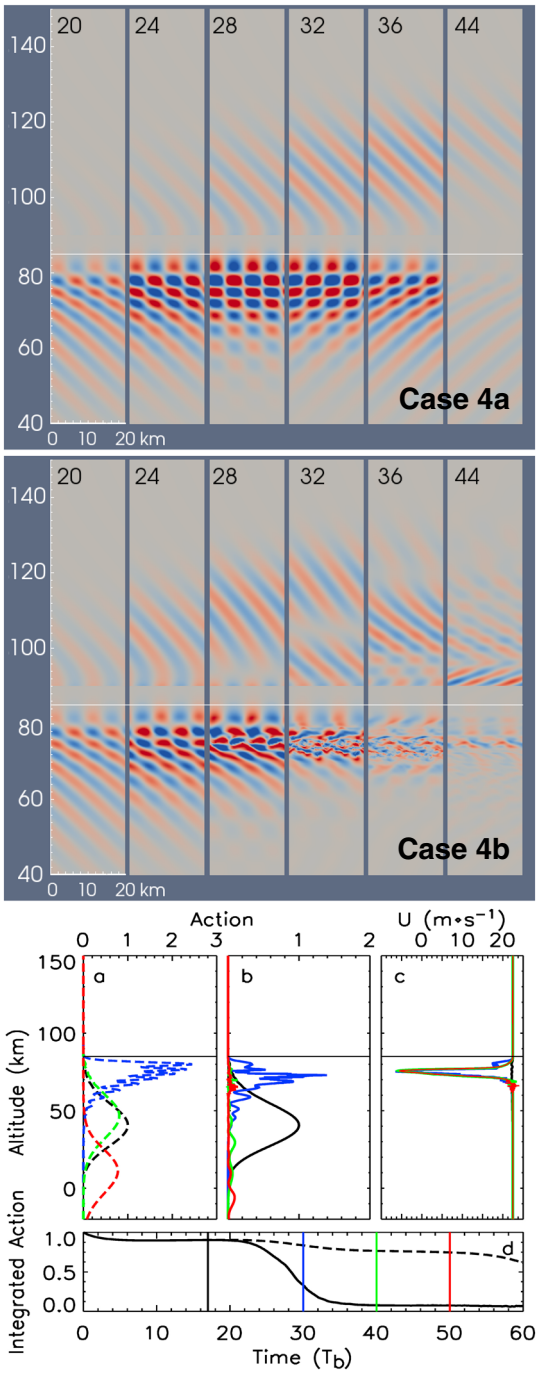

Figure 9. As in Figure 7 for Cases 4a and 4b with cross sections at 20, 24, 28, 32, 36, and 44 T_b and contour limits of ±0.1 and 10 m s^{-1}, respectively. The contour scales are reduced by factors of 10 and 40 for Cases 4a and 4b, respectively, above 90 km in order to reveal the weaker amplitudes.

85 km. Hence, a 10 times smaller color scale range is employed above 90 km that enables these weak responses to be seen for both cases.

Due to the long residence times in the MIL, the GW amplitudes in the MIL for the two cases increase strongly in time, achieving maxima at ~30 and 28 T_b, respectively. The reflected GW in Case 4a is dominated by the incident GW prior to the peak MIL amplitude at ~28 T_b, but dominates thereafter. The reflected GW in Case 4b is strongly suppressed by instabilities and dissipation in the MIL throughout the evolution.

Transmitted and/or radiated GW fields above the MIL highlighted by the enhanced color scale above 90 km reveal weak transmission extending beyond 36 T_b in Case 4a and comparable transmission prior to strong instabilities in Case 4b. Instability dynamics in the MIL in Case 4b beginning before 28 T_b radiate secondary GWs to higher and lower altitudes that have both upstream (upward to the left) and downstream (upward to the right) phase alignments above the MIL thereafter. These achieve larger amplitudes below than above the MIL, and those propagating upward and downstream above the MIL have smaller λ_z due to their much smaller $|c - U|$ relative to the GWs in the MIL and above propagating upstream (leftward) at $c > U$, see equation (1), because of the strong induced mean wind shear above the MIL (see Figure 9c at bottom).

GW $A(z)$ profiles in Case 4a (Figure 9a at bottom) reveal nearly total GW reflection, though the peak $A(z)$ at 30 T_b and thereafter is reduced due to transient residence in the MIL leading to a longer reflected GW packet. The $A(z)$ profiles for Case 4b (Figure 9b at bottom) likewise reveal weak transmission, but significant trapping and partial dissipation in the MIL at 30 T_b and stronger dissipation and weak reflection thereafter. The $U(z)$ profiles reveal the rapid evolution of a MIL jet by 30 T_b that remains fairly uniform as the GW dissipates in the MIL. The induced $U(z)$ achieves a maximum ~28 m s^{-1} and a FWHM ~4 km. Though weaker than the jets achieved with a MIL in Cases 2 and 3, the peak U in Case 4b is likewise ~30% larger than the initial GW initial phase speed.

3.5. Linear and Nonlinear Responses for λ_x = 20 km, λ_{z0} = 10 km, and β = 1

Cases 5a and 5b (see Table 1) describing MIL responses for linear and nonlinear GWs having λ_x = 20 km, λ_{z0} = 10 km, and β = 1 are illustrated with streamwise cross sections of u' from 20 to 44 T_b in Figure 10 (top and middle), respectively. Case 5a most closely resembles Cases 1c and 3a (having λ_{z0} = 20 and 40 km, respectively). In Case 5a, however, transient trapping in the MIL is followed by measurably larger (a few %) transmission, but still nearly total reflection, though on longer time scales in Case 5a due to the much larger c_{gz} in Cases 1c and 3a. For example, compare the GW u' cross sections and the $A(z)$ and $U(z)$ profiles in Figures 2 and 7 with those for Case 5a in Figure 10.

Similarly, Case 5b most closely resembles Cases 2b and 3b, apart from the much larger λ_{z0} and c_{gz} in the earlier cases and the enhanced transmission seen in Case 5a. Compression of λ_z in Case 5b by ~1.5 at the peak N^2 again contributes to increased du'/dz in the MIL and instability dynamics beginning between ~28 T_b and rapid GW dissipation and cessation of GW transmission and reflection thereafter. As in all the nonlinear cases discussed above, Case 5b yields an induced $U(z)$ in the MIL having a maximum ~35 m s^{-1}, thus also ~30% above the initial GW c. The more significant transmission in Case 5b, though small, enables significantly stronger forcing at higher altitudes than

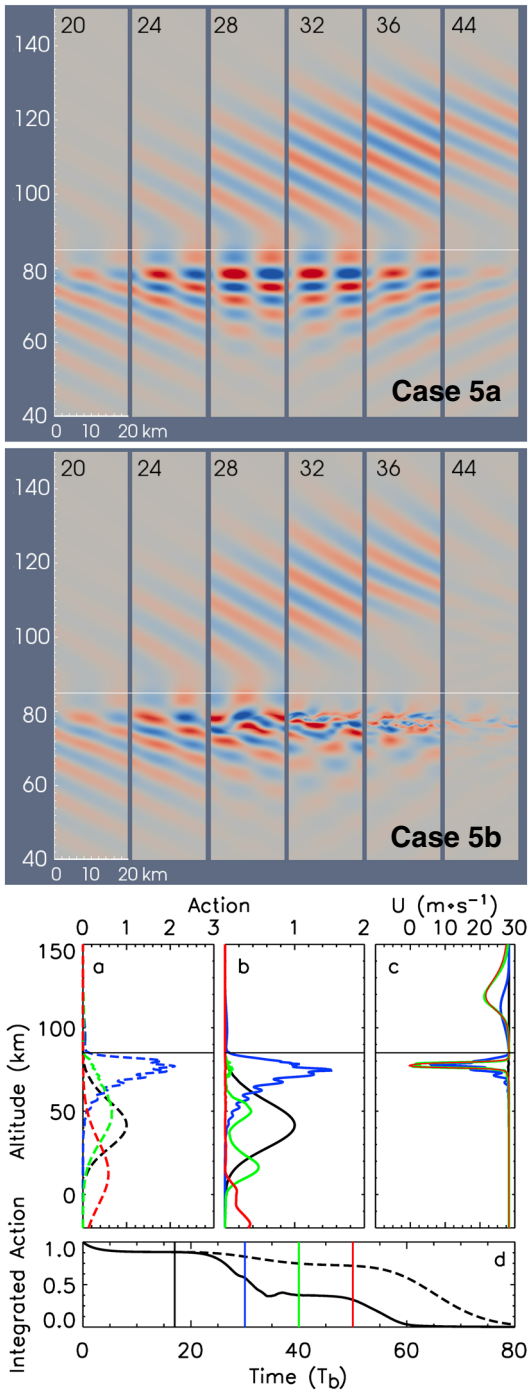

Figure 10. As in Figure 9 for Cases 5a and 5b with contour limits of ±0.2 and 20 m s^{-1}, respectively.

seen in Cases 2b and 3b, despite their stronger forcing at the MIL. However, this is applied at a lower altitude in Case 5b by ~15 km due to smaller c_{gz} in this case (~120 rather than ~135 km). As in Cases 2b and 3b, the transmitted and reflected responses are essentially truncated versions of the corresponding linear results due to the occurrence of instabilities and turbulence that reduce GW transmission and reflection thereafter.

3.6. Linear and Nonlinear Responses for λ_x = 40 km, λ_{z0} = 20 km, and β = 1

We now compare the responses for linear and nonlinear GWs having λ_x = 40 km, λ_{z0} = 20 km, and β = 1 (Cases 6a and 6b, see Table 1) with those having λ_x = 20 km (Cases 1c and 2b). Streamwise u' cross sections for Cases 6a and 6b are shown from 10 to 26 T_b in Figure 11 (top and middle). As in the comparisons described for Cases 5a and 5b above, those here exhibit differences from Cases 1c and 2b that can be largely attributed to the smaller GW c_{gz} and the more efficient transmission for the more hydrostatic GWs in Cases 6a and 6b (due to the less negative m^2 at altitudes with small N^2). The smaller GW c_{gz} causes slightly delayed MIL dynamics in Cases 6a and 6b relative to Cases 1c and 2b. Specifically, transmitted and reflected GWs arise slightly later and are excited over longer intervals in Cases 6a and 6b than in Cases 1c and 2b due to the longer residence in the MIL in Cases 6a and 6b.

Considering first the linear cases, the u' cross sections for Case 6a reveal dramatically stronger transmission than for Case 1c, relative to the reflected GW below the MIL, which implied a transmitted peak $A \sim 0.003$. In comparison, Case 6a exhibits a peak $A \sim 0.2$ above the MIL at 15 T_b. This much stronger transmission enables large relative amplitudes extending to high altitudes. But due to the small initial GW amplitude, there is no indication of nonlinear SA dynamics such as seen in Case 2a. Case 6a transmission is also significantly stronger than that in Case 5a that has the same ω_i, but λ_x and λ_{z0} half as large. Larger λ_{z0} in Case 6a implies smaller negative $m^2 \sim -k^2$ due to $N \sim 0$ above the MIL, hence enhanced transmission across the evanescent layer relative to Case 5a, as observed.

Case 6b likewise has an initial transmitted $A \sim 0.2$, but this GW decreases strongly with altitude and time thereafter (see the u' cross sections at 22 and 26 T_b in Figure 11 and subpanel b at bottom). The reason is that the much larger Case 6b initial GW amplitude yields a transmitted GW that has a large momentum flux and yields strong dU/dt at altitudes of ~100 km and above beginning prior to 15 T_b. This induces rapidly accelerating $U(z)$ at the GW packet leading edge and large dU/dz at the packet trailing edge (see the $U(z)$ profiles in Figure 11c at bottom). These responses are characteristics of SA dynamics driving GW phase kinking, λ_z compression, SA instabilities, and GW breakdown thereafter, as seen accompanying the GW reaching high altitudes in Case 2a.

Returning to the u' cross sections for Case 6b, we see strong modulations of the GW in the MIL, as in the nonlinear cases above, but only very weak, small-scale structures arise. This indicates that despite a tendency for instabilities and GW breaking in the MIL, these are weak influences. Instead, the $A(z)$ profiles for Case 6b reveal that there is also strong reflection in this case, with only a relatively small fraction of integrated A dissipated in the MIL. This explains the relatively small-induced $U(z)$ remaining in the MIL

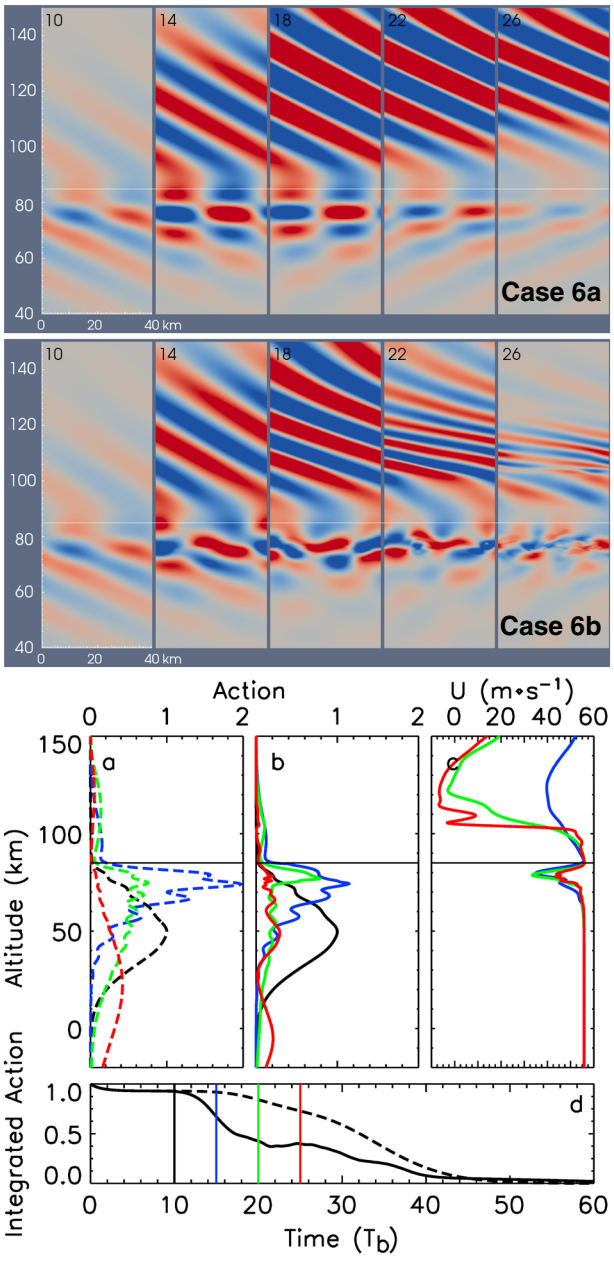

Figure 11. As in Figure 9 for Cases 6a and 6b with profiles at 10, 14, 18, 22, and 26 T_b and contour limits of ±0.2 and 20 m s^{-1}, respectively.

at late stages of the evolution, e.g., a maximum $U \sim 12$ m s^{-1} (relative to the initial $c \sim 44$ m s^{-1}). This is in sharp contrast with those cases having strong dissipation that yielded a maximum U in the MIL ~30% larger than c).

4. Summary and Discussion

As noted above, satellite, ground-based, and in situ observations have been interpreted as evidence of MILs at altitudes from the stratosphere into the lower thermosphere for many years. Large-scale MILs extending large distances in satellite observations or descending slowly with the phase of tidal motions have been attributed to PW structure near a zero-wind line (or critical level) or large-amplitude tides that may or may not involve GW-tidal interactions (e.g., Meriwether & Gerrard, 2004; Oberheide et al., 2006; Salby et al., 2002; Williams et al., 2006). Other observations by lidars and/or in situ probes in the stratosphere and mesosphere have identified regions of positive dT/dz as MILs, often with nearly adiabatic layers above, that may or may not include tidal contributions. In many cases, however, these are more likely associated with large-amplitude GWs at various vertical scales (e.g., Fritts et al., 2004; Goldberg et al., 2006; Hauchecorne et al., 1987; Lehmacher et al., 2006; Szewczyk et al., 2013; Whiteway et al., 1995), rather than with true MILs in the absence of GW perturbations. As an example, a breaking GW will exhibit a dT/dz with alternating strong positive and superadiabatic phases, and correlations of instabilities and turbulence with the most unstable phase of the GW (including the GW wind shears). Importantly, such GW-induced "MILs" and related dynamics extend to much lower altitudes, though with decreasing magnitudes and vertical scales, as evidenced by the ubiquity of S&L structures throughout the lower atmosphere (e.g., Fritts et al., 2016, and references therein). Other features that exhibit similar dynamics to MILs include climatological inversions capping the tropopause and the polar summer mesopause.

Implications of the above discussion are that there is a continuum of related dynamics that extends from large-scale MILs that are local mean structures such as driven by PWs near critical levels, to positive dT/dz due to large-amplitude tides, to GW-tidal interactions, and finally to individual or superposed GWs yielding multiple regions of strong positive dT/dz on various spatial and temporal scales. The latter include (1) S&L structures and their associated instabilities and mixing at larger GW amplitudes and (2) smaller-scale and smaller-amplitude GWs propagating in larger-scale GW environments. Smaller-amplitude cases have been studied by multiple authors to date (e.g., Broutman et al., 1997; Broutman & Young, 1986; Dunkerton, 1987; Eckermann, 1997, 1999; Heale & Snively, 2015; Vanneste, 1995; Walterscheid, 2000). These reveal that a small-scale GW propagating through a larger-scale GW, or more general GW superpositions, can yield significant departures from the predictions of GW propagation in a steady, slowly varying sheared and stratified environment. Effects include refraction to smaller and larger scales, partial or total reflection, tunneling through evanescent regions, avoidance of critical-level dissipation, wave-wave interactions, intensification of amplitudes and shears, and initiation of instabilities and turbulence.

Our simulation results described above include the following:

1. MILs for $b = 1$ and $z_{MIL} \sim 10$ km (minimum and maximum N^2 of 0 and $2N_0^2$) impose nearly complete reflection for GWs with $\lambda_x = 10$ and 20 km and $\lambda_z = 10$, 20, and 40 km.

2. MIL transmission for these GW parameters, while small, is enhanced for larger λ_z and for more hydrostatic GWs at the same λ_z (i.e., larger λ_x).
3. GW trapping and residence in a MIL are prolonged for GW λ_z and $\lambda_x \sim z_{MIL}$ or less.
4. MILs intensify GW amplitudes and shears that can enable instabilities, turbulence, and GW dissipation at sufficient amplitudes.
5. GW dissipation in a MIL yields energy and momentum deposition, jet formation, and reduced transmission and reflection.
6. The 3-D simulations for cases with strong instability dynamics showed the corresponding nonphysical 2-D simulations to yield approximately the same 2-D GW fields and the associated transmission and reflection in wave action density.

We believe that our idealized simulations with GW packets confined only in altitude capture the local MIL dynamics listed above very well. However, they cannot address the larger-scale responses that must accompany a GW packet localized in 3-D. In reality, all GW packets are 3-D, with horizontal scales that are dictated by their sources, horizontal wavelengths, and propagation and dispersion above their sources. Such packets induce spatially localized momentum deposition and mean flow accelerations that induce immediate, but slowly evolving, compensating horizontal and vertical circulations. The time scale for this adjustment is dictated by the depth to the width of the induced mean flow (Luo & Fritts, 1993; Plougonven & Zhang, 2014; Vadas & Fritts, 2001). Assuming our Case 2 or Case 3 GW with λ_x = 20 km, a typical GW packet width of ~3–5 λ_x ~ 60–100 km, and the induced mean wind jet depth of ~3 km implies a width-to-depth ratio of ~20 to 30 and evolution timescale of ~20 to 30 T_b. This range is significantly longer than the interval over which strong mean-flow accelerations occur in Cases 2 and 3 (~5 T_b), suggesting that the mean flow adjustment would largely impact the late stages of 3-D versions of these dynamics.

Our choices for GW parameters were made in part to enable rapid momentum transports, mean flow evolutions, and energetic instability and turbulence evolutions allowing efficient numerical computation. As a result, the induced mean flows are larger than would arise for smaller-amplitude, more hydrostatic GWs, and significant mean flow accelerations within a MIL have yet to be observed. Given that the ducted GWs are embedded in the MIL jet structures in these cases, it is possible that the larger mean motions contribute to the trapping to some degree.

Another consequence of our parameter choice for Cases 3b and 3c is the potential for modulational instability, which arises for GWs having $\lambda_z/\lambda_x > 2^{1/2}[1 + 1/(2kH)^2]^{-1/2}$ for sufficiently large GW amplitudes in an anelastic atmosphere (Dosser & Sutherland, 2011). Modulational instability appears not to occur in our Cases 3b and 3c simulations, however. This is because $(\lambda_z/\lambda_x)^2 = 4$ initially (with $N^2/\omega_i^2 \approx 1.25$) but decreases to $(\lambda_z/\lambda_x)^2 \sim 2$ (with $N^2/\omega_i^2 \approx 1.5$) at ~65 km, above which modulational instability is no longer possible and below which the GW amplitude is well below that for which modulational instability has been modeled.

The implications of these results for GW propagation and dissipation are many. Compared to an environment without a MIL, a single MIL yields partial to near-total GW reflection, depending on the MIL strength and GW parameters. It also implies a tendency for GW dissipation below where it would otherwise occur and additional reductions in both transmitted and reflected GWs. Multiple apparent MILs, such as would accompany a large-amplitude, larger-scale GW or a strong S&L environment due to superposed multiscale GWs, suggest many such GW interactions yielding (1) a spreading and/or randomization of GW fluxes of energy and momentum to higher altitudes and (2) more frequent GW dissipation events that may be more uniformly or widely distributed in altitude than predicted by models or theory accounting for only a few dominant components of the GW spectrum in less structured environments. Indeed, such dynamics provide strong underpinning for GW parameterizations based on the nonlinear dynamics of interacting GWs throughout the atmosphere.

5. Conclusions

Our modeling results have provided insights into the dynamics of GWs encountering mesosphere inversion layers (MILs), and similar climatological or transient structures at lower and higher altitudes. We examined idealized cases in which the "MIL" comprises a layer of elevated N^2 with a layer of reduced (or zero) N^2 above that are separated by z_{MIL} ~ 10 km for GWs assumed to have λ_x and λ_z of 10–40 km in various combinations.

Larger-scale GWs were more likely to be transmitted by the MIL, if they were not induced to exhibit instabilities in the MIL. Smaller-scale GWs were found to exhibit even less transmission due to their greater evanescence in the weak N^2 layer above the MIL. Where instabilities occurred, they further reduced transmission and reflection. We expect these results to also have applicability to other MIL and GW scales exhibiting similar relations.

Related studies of small-scale GW propagation within a larger-scale GW suggest that multiple effective MILs due to superposed multiscale GWs would (1) cause GW vertical fluxes of energy and momentum to become more stochastic and uniform, as opposed to discrete and episodic, and (2) result in GW dissipation that is also more uniformly varying in altitude (though potentially very structured at small scales). Similar dynamics and implications also accompany more general multiscale dynamics throughout the atmosphere. Such effects are implicit in parameterizations of GW influences that are based on spectral descriptions of the GW field (e.g., Fritts & VanZandt, 1993; Hines, 1997; Medvedev & Klaassen, 1995; Warner & McIntyre, 2001; Yiğit et al., 2008), especially re-population of the spectrum by secondary GW generation, that is not accounted for in more "linear" and discrete GW schemes.

Additional studies are needed that address a broader range of GW scales and frequencies in environments having more realistic multiscale backgrounds. The challenge will be to more fully understand the dynamics underlying the ~3 decade decrease of GW energy from the troposphere to the mesopause and their implications for GW-induced forcing, transport, and the evolution of the GW spectrum from low altitudes into the thermosphere.

Acknowledgments
Research described here was performed under NASA, National Science Foundation, and ONR grants or contracts cited in GEMS. We also acknowledge the DoD High Performance Computing Modernization Program (HPCMP) for valuable access to several supercomputer platforms that allowed the simulations reported here. The individual 3-D numerical data sets spanning the durations of our various simulations are too large to be retrieved from the DoD HPCMP centers. Given this, all 2-D data fields employed to create the figures in this paper are included as supplemental data linked to this paper.

References

Achatz, U. (2005). On the role of optimal perturbations in the instability of monochromatic gravity waves. *Physics of Fluids*, *17*(9), 094107. https://doi.org/10.1063/1.2046709

Achatz, U. (2007). The primary nonlinear dynamics of modal and nonmodal perturbations of monochromatic inertia-gravity waves. *Journal of the Atmospheric Sciences*, *64*(1), 74–95. https://doi.org/10.1175/JAS3827.1

Balsley, B. B., Frehlich, R. G., Jensen, M. L., Meillier, Y., & Muschinski, A. (2003). Extreme gradients in the nocturnal boundary layer: Structure, evolution, and potential causes. *Journal of the Atmospheric Sciences*, *60*(20), 2496–2508. https://doi.org/10.1175/1520-0469(2003)060%3C2496:EGITNB%3E2.0.CO;2

Balsley, B. B., Jensen, M. L., & Frehlich, R. (1998). The use of state-of-the-art kites for profiling the lower atmosphere. *Boundary-Layer Meteorology*, *87*(1), 1–25. https://doi.org/10.1023/A:1000812511429

Balsley, B. B., Lawrence, D. A., Woodman, R. F., & Fritts, D. C. (2013). Fine-scale characteristics of temperature, wind, and turbulence in the lower atmosphere (0-1,300 m) over the south Peruvian coast. *Boundary-Layer Meteorology*, *147*(1), 165–178. https://doi.org/10.1007/s10546-012-9774-x

Bannon, P. (1996). On the anelastic approximation for a compressible atmosphere. *Journal of the Atmospheric Sciences*, *53*(23), 3618–3628. https://doi.org/10.1175/1520-0469(1996)053%3C3618:OTAAFA%3E2.0.CO;2

Baumgarten, G., Chandran, A., Fiedler, J., Hoffmann, P., Kaifler, N., Lumpe, J., … Thomas, G. (2012). On the horizontal and temporal structure of noctilucent clouds as observed by satellite and lidar at ALOMAR (69N). *Geophysical Research Letters*, *39*, L01803. https://doi.org/10.1029/2011GL049935

Baumgarten, G., & Fritts, D. C. (2014). Quantifying Kelvin-Helmholtz instability dynamics observed in noctilucent clouds: 1. Methods and observations. *Journal of Geophysical Research: Atmospheres*, *119*, 9324–9337. https://doi.org/10.1002/2014JD021832

Bell, S. W., & Geller, M. A. (2008). The tropopause inversion layer: Seasonal and latitudinal variations, representation in standard radiosonde data and global models. *Journal of Geophysical Research*, *113*, D05109. https://doi.org/10.1029/2007/JD009022

Birner, T. (2006). Fine-scale structure of the extratropical tropopause region. *Journal of Geophysical Research*, *111*, D04104. https://doi.org/10.1029/2005JD006301

Birner, T., Dörnbrack, A., & Schumann, U. (2002). How sharp is the tropical tropopause? *Geophysical Research Letters*, *29*(14), 1700. https://doi.org/10.1029/2002GL015142

Blumen, W., Banta, R., Burns, S. P., Fritts, D. C., Newsom, R., Poulos, G. S., & Sun, J. (2001). Turbulence statistics of a Kelvin-Helmholtz billow event observed in the nighttime boundary layer during the CASES-99 field program. *Dynamics of Atmospheres and Oceans*, *34*, 189–204.

Broutman, D., MaCaskill, C., McIntyre, M. E., & Rottman, J. W. (1997). On Doppler-spreading models of internal waves. *Geophysical Research Letters*, *24*(22), 2813–2816. https://doi.org/10.1029/97GL52902

Broutman, D., & Young, W. R. (1986). On the interaction of small-scale internal waves with near-inertial waves. *Journal of Fluid Mechanics*, *166*, 341–358. https://doi.org/10.1017/S0022112086000186

Chao, W. C., & Schoeberl, M. R. (1984). On the linear approximation of gravity wave saturation in the mesosphere. *Journal of the Atmospheric Sciences*, *41*(11), 1893–1898. https://doi.org/10.1175/1520-0469(1984)041%3C1893:OTLAOG%3E2.0.CO;2

Chen, W. N., Tsao, C. C., & Nee, J. B. (2004). Rayleigh lidar temperature measurements in the upper troposphere and lower stratosphere. *Journal of Atmospheric and Solar: Terrestrial Physics*, *66*, 39–49.

Chuda, T., Kimura, R., & Niino, H. (2007). Vertical fine structures of temperature and water vapor in the free atmosphere. *Journal of the Meteorological Society of Japan*, *85*(5), 583–597. https://doi.org/10.2151/jmsj.85.583

Clancy, R. T., Rush, D. W., & Callan, M. T. (1994). Temperature minima in the average thermal structure of the middle atmosphere (70–80 km) from analysis of 40- to 92-km SME global temperature profiles. *Journal of Geophysical Research*, *99*(D9), 19,001–19,020. https://doi.org/10.1029/94JD01681

Collins, R. L., Lehmacher, G. A., Larsen, M. F., & Mizutani, K. (2011). Estimates of vertical eddy diffusivity in the upper mesosphere in the presence of a mesospheric inversion layer. *Annales Geophysicae*, *29*(11), 2019–2029. https://doi.org/10.5194/angeo-29-2019-2011

Coulman, C. E. (1973). Vertical profiles of small-scale temperature structure in the atmosphere. *Boundary-Layer Meteorology*, *4*(1-4), 169–177. https://doi.org/10.1007/BF02265230

Coulman, C. E., Vernin, J., & Fuchs, A. (1995). Optical seeing mechanism of formation of thin turbulent laminae in the atmosphere. *Applied Optics*, *34*(24), 5461–5474. https://doi.org/10.1364/AO.34.005461

Coy, L., & Fritts, D. C. (1988). Gravity wave heat fluxes: A Lagrangian approach. *Journal of the Atmospheric Sciences*, *45*(12), 1770–1780. https://doi.org/10.1175/1520-0469(1988)045%3C1770:GWLFAL%3E2.0.CO;2

Cutler, L. J., Collins, R. L., Mizutani, K., & Itabe, T. (2001). Rayleigh lidar observations of mesospheric inversion layers at Poker Flat, Alaska (65°N, 147°W). *Geophysical Research Letters*, *28*(8), 1467–1470. https://doi.org/10.1029/2000GL012535

Dalaudier, F., Sidi, C., Crochet, M., & Vernin, J. (1994). Direct evidence of "sheets" in the atmospheric temperature field. *Journal of the Atmospheric Sciences*, *51*(2), 237–248. https://doi.org/10.1175/1520-0469(1994)051%3C0237:DEOITA%3E2.0.CO;2

Dao, P. D., Farley, R., Tao, X., & Gardner, C. S. (1995). Lidar observations of the temperature profile between 25 and 103 km: Evidence of strong tidal perturbation. *Geophysical Research Letters*, *22*(20), 2825–2828. https://doi.org/10.1029/95GL02950

Dosser, H. V., & Sutherland, B. R. (2011). Weakly nonlinear non-Boussinesq internal gravity wavepackets. *Physica D*, *240*(3), 346–356. https://doi.org/10.1016/j.physd.2010.09.008

Duck, T. J., Sipler, D. P., Salah, J. E., & Meriwether, J. W. (2001). Rayleigh lidar observations of a mesospheric inversion layer during night and day. *Geophysical Research Letters*, *28*(18), 3597–3600. https://doi.org/10.1029/2001GL013409

Dunkerton, T. J. (1987). Effect of nonlinear instability on gravity wave momentum transport. *Journal of the Atmospheric Sciences*, *44*(21), 3188–3209. https://doi.org/10.1175/1520-0469(1987)044%3C3188:EONIOG%3E2.0.CO;2

Dunkerton, T. J., & Fritts, D. C. (1984). Transient gravity wave-critical level interaction. Part I: Convective adjustment and the mean zonal acceleration. *Journal of the Atmospheric Sciences*, *41*(6), 992–1007. https://doi.org/10.1175/1520-0469(1984)041%3C0992:TGWCLI%3E2.0.CO;2

Eckermann, S. D. (1997). Influence of wave propagation on the Doppler-spreading of atmospheric gravity waves. *Journal of the Atmospheric Sciences*, *54*(21), 2554–2573. https://doi.org/10.1175/1520-0469(1997)054%3C2554:IOWPOT%3E2.0.CO;2

Eckermann, S. D. (1999). Isentropic advection by gravity waves: Quasi-universal M%3 vertical wavenumber spectra near the onset of instability. *Geophysical Research Letters*, *26*(2), 201–204. https://doi.org/10.1029/1998GL900283

Fechine, J., Wrasse, C. M., Takahashi, H., Mlynczak, M. G., & Russell, J. M. (2008). Lower-mesospheric inversion layers over Brazilian equatorial region using TIMED/SABER temperature profiles. *Advances in Space Research*, *41*(9), 1447–1453. https://doi.org/10.1016/j.asr.2007.04.070

Felten, F. N., & Lund, T. S. (2006). Kinetic energy conservation issues associated with the collocated mesh scheme for incompressible flow. *Journal of Computational Physics*, *215*(2), 465–484. https://doi.org/10.1016/j.jcp.2005.11.009

France, J. A., Harvey, V. L., Randall, C. E., Collins, R. L., Smith, A. K., Peck, E. D., & Fang, X. (2015). A climatology of planetary wave-driven mesospheric inversion layers in the extratropical winter. *Journal of Geophysical Research: Atmospheres*, *120*, 399–413. https://doi.org/10.1002/2014JD022244

Fritts, D. C., & Alexander, M. J. (2003). Gravity dynamics and effects in the middle atmosphere, *Reviews of Geophysics*, *41*(1), 1003. https://doi.org/10.1029/2001RG000106

Fritts, D. C., Baumgarten, G., Wan, K., Werne, J. A., & Lund, T. (2014). Quantifying Kelvin-Helmholtz instability dynamics observed in noctilucent clouds: 2. Modeling and interpretation of observations. *Journal of Geophysical Research: Atmospheres*, *119*, 9359–9359. https://doi.org/10.1002/2014JD021833

Fritts, D. C., & Dunkerton, T. J. (1985). Fluxes of heat and constituents due to convectively unstable gravity waves. *Journal of the Atmospheric Sciences*, *42*(6), 549–556. https://doi.org/10.1175/1520-0469(1985)042%3C0549:FOHACD%3E2.0.CO;2

Fritts, D. C., Laughman, B., Lund, T. S., & Snively, J. B. (2015). Self-acceleration and instability of gravity wave packets: 1. Effects of temporal localization. *Journal of Geophysical Research: Atmospheres*, *120*, 8783–8803. https://doi.org/10.1002/2015JD023363

Fritts, D. C., & VanZandt, T. E. (1993). Spectral estimates of gravity wave energy and momentum fluxes, I. Energy dissipation, acceleration, and constraints. *Journal of the Atmospheric Sciences*, *50*(22), 3685–3694. https://doi.org/10.1175/1520-0469(1993)050%3C3685:SEOGWE%3E2.0.CO;2

Fritts, D. C., Wan, K., Franke, P., & Lund, T. (2012). Computation of clear-air radar backscatter from numerical simulations of turbulence, 3. Off-zenith measurements and biases throughout the lifecycle of a Kelvin-Helmholtz instability. *Journal of Geophysical Research*, *117*, D17101. https://doi.org/10.1029/2011JD017179

Fritts, D. C., & Wang, L. (2013). Gravity wave–dine structure interactions. Part 2: Energy dissipation evolutions, statistics, and implications. *Journal of the Atmospheric Sciences*, *70*(12), 3735–3755. https://doi.org/10.1175/JAS-D-13-059.1

Fritts, D. C., Wang, L., Baumgarten, G., Miller, A. D., Geller, M. A., Jones, G., … Vinokurov, J. (2017). High-resolution observations and modeling of turbulence sources, structures, and intensities in the upper mesosphere. *Journal of Atmospheric and Solar - Terrestrial Physics*, *162*, 57–78. https://doi.org/10.1016/j.jastp.2016.11.006

Fritts, D. C., Wang, L., Laughman, B., Lund, T. S., & Collins, R. L. (2017). Gravity Wave Dynamics in a Mesospheric Inversion Layer: 2. Instabilities, Turbulence, Fluxes, and Mixing. *Journal of Geophysical Research: Atmospheres*, *122*. https://doi.org/10.1002/2017JD027442

Fritts, D. C., Wang, L., Geller, M. A., Lawrence, D. A., Werne, J., & Balsley, B. B. (2016). Numerical modeling of multi-scale dynamics at a high Reynolds number: Instabilities, turbulence, and an assessment of Ozmidov and Thorpe scales. *Journal of the Atmospheric Sciences*, *73*(2), 555–578. https://doi.org/10.1175/JAS-D-14-0343.1

Fritts, D. C., Wang, L., & Werne, J. (2013). Gravity wave–fine structure interactions. Part 1: Influences of fine structure form and orientation on flow evolution and instability. *Journal of the Atmospheric Sciences*, *70*(12), 3710–3734. https://doi.org/10.1175/JAS-D-13-055.1

Fritts, D. C., Wang, L., Werne, J., Lund, T., & Wan, K. (2009a). Gravity wave instability dynamics at high Reynolds numbers, 1: Wave field evolution at large amplitudes and high frequencies. *Journal of the Atmospheric Sciences*, *66*(5), 1126–1148. https://doi.org/10.1175/2008JAS2726.1

Fritts, D. C., Wang, L., Werne, J., Lund, T., & Wan, K. (2009b). Gravity wave instability dynamics at high Reynolds numbers, 2: Turbulence evolution, structure, and anisotropy. *Journal of the Atmospheric Sciences*, *66*(5), 1149–1171. https://doi.org/10.1175/2008JAS2727.1

Fritts, D. C., Williams, B. P., She, C.-Y., Vance, J. D., Rapp, M., Lübken, F.-J., … Goldberg, R. A. (2004). Observations of extreme temperature and wind gradients near the summer mesopause during the MaCWAVE/MIDAS rocket campaign. *Geophysical Research Letters*, *31*, L24S06. https://doi.org/10.1029/2003GL019389

Fukao, S., Luce, H., Mega, T., & Yamamoto, M. (2011). Extensive studies of large-amplitude Kelvin–Helmholtz billows in the lower atmosphere with VHF middle and upper atmosphere radar. *Quarterly Journal of the Royal Meteorological Society*, *137*(657), 1019–1041. https://doi.org/10.1002/qj.807

Gan, Q., Zhang, S. D., & Yi, F. (2012). TIMED/SABER observations of lower mesospheric inversion layers at low and middle latitudes. *Journal of Geophysical Research*, *117*, D07109. https://doi.org/10.1029/2012JD017455

Germano, M., Piomelli, U., Moin, P., & Cabot, W. H. (1991). A dynamic subgrid-scale eddy viscosity model. *Physics of Fluids A*, *3*(7), 1760–1765. https://doi.org/10.1063/1.857955

Gisinger, S., Dörnbrack, A., Matthias, V., Doyle, J. D., Eckermann, S. D., Ehard, B., … Rapp, M. (2017). Atmospheric conditions during the Deep Propagating Gravity Wave Experiment (DEEPWAVE). *Monthly Weather Review*, *145*(10), 4249–4275. https://doi.org/10.1175/MWR-D-16-0435.1

Goldberg, R. A., Fritts, D. C., Schmidlin, F. J., Williams, B. P., Croskey, C. L., Mitchell, J. D., … Blum, U. (2006). The MaCWAVE program to study gravity wave influences on the polar mesosphere. *Annales Geophysicae*, *24*(4), 1159–1173. https://doi.org/10.5194/angeo-24-1159-2006

Gossard, E. E., Gaynor, J. E., Zamora, R. J., & Neff, W. D. (1985). Fine structure of elevated stable layers observed by sounder and in-situ tower sensors. *Journal of the Atmospheric Sciences*, *42*(20), 2156–2169. https://doi.org/10.1175/1520-0469(1985)042%3C2156:FOESLO%3E2.0.CO;2

Hauchecorne, A., & Chanin, M. L. (1980). Density and temperature profiles obtained by lidar between 35 and 70 km. *Geophysical Research Letters*, *7*(8), 565–568. https://doi.org/10.1029/GL007i008p00565

Hauchecorne, A., Chanin, M. L., & Wilson, R. (1987). Mesospheric temperature inversion and gravity wave dynamics. *Geophysical Research Letters*, *14*, 935–939.

Heale, C. J., & Snively, J. B. (2015). Gravity wave propagation through a vertically and horizontally inhomogeneous background wind. *Journal of Geophysical Research: Atmospheres*, *120*, 5931–5950. https://doi.org/10.1002/2015JD023505

Hecht, J. H., Wan, K., Gelinas, L. J., Fritts, D. C., Walterscheid, R. L., Franke, S. J., … Pautet, P. D. (2014). The lifecycle of instability features measured from the Andes Lidar Observatory over Cerro Pachon on March 24, 2012. *Journal of Geophysical Research: Atmospheres*, *119*, 8872–8898. https://doi.org/10.1002/2014JD021726

Hines, C. O. (1997). Doppler-spread parameterization of gravity-wave momentum deposition in the middle atmosphere, 1. Basic formulation. *Journal of Atmospheric and Solar - Terrestrial Physics*, *59*(4), 371–386. https://doi.org/10.1016/S1364-6826(96)00079-X

Irving, B. K., Collins, R. L., Lieberman, R. S., Thurairajah, B., & Mizutani, K. (2014). Mesospheric inversion layers at Chatanika, Alaska (65°N, 147°W): Rayleigh lidar observations and analysis. *Journal of Geophysical Research: Atmospheres*, *119*, 11,235–11,249. https://doi.org/10.1002/2014JD021838

Keckhut, P., Chanin, M. L., & Hauchecorne, A. (1990). Stratosphere temperature measurement using Raman lidar. *Applied Optics*, *29*(34), 5182–5186. https://doi.org/10.1364/AO.29.005182

Kim, Y.-J., Eckermann, S. D., & Chun, H.-Y. (2003). A overview of the past, present and future of gravity-wave drag parameterization for numerical climate and weather prediction models. *Atmosphere-Ocean*, *41*, 65–98.

Kumar, V. S., Kumar, Y. B., Raghunath, K., Rao, R. B., Krishnaiah, M., Mizutani, K., … Itabe, T. (2001). Lidar measurements of mesospheric temperature inversion at a low latitude. *Annales Geophysicae*, *19*(8), 1039–1044. https://doi.org/10.5194/angeo-19-1039-2001

Leblanc, T., & Hauchecorne, A. (1997). Recent observations of mesospheric temperature inversions. *Journal of Geophysical Research*, *102*(D16), 19,471–19,482. https://doi.org/10.1029/97JD01445

Leblanc, T., Hauchecorne, A., Chanin, M. L., Taylor, F. W., Rodgers, C. D., & Livesey, N. (1995). Mesospheric temperature inversions as seen by ISAMS (UARS). *Geophysical Research Letters*, *22*(12), 1485–1488. https://doi.org/10.1029/94GL03274

Lehmacher, G., Croskey, C. L., Mitchell, J. D., Friedrich, M., Lübken, F.-J., Rapp, M., … Fritts, D. C. (2006). Intense turbulence observed above a mesospheric temperature inversion at equatorial latitude. *Geophysical Research Letters*, *33*, L08808. https://doi.org/10.1029/2005GL024345

Lehmacher, G., & Lübken, F.-J. (1995). Simultaneous observation of convective adjustment and turbulence generation in the mesosphere. *Geophysical Research Letters*, *22*(18), 2477–2480. https://doi.org/10.1029/95GL02351

Lehmacher, G. A., Scott, T. D., Larsen, M. F., Bilen, S. G., Croskey, C. L., Mitchell, J. D., … Collins, R. L. (2011). The Turbopause experiment: Atmospheric stability and turbulent structure spanning the turbopause altitude. *Annales Geophysicae*, *29*(12), 2327–2339. https://doi.org/10.5194/angeo-29-2327-2011

Lelong, M.-P., & Dunkerton, T. J. (1998a). Inertia–gravity wave breaking in three dimensions. Part I: Convectively stable waves. *Journal of the Atmospheric Sciences*, *55*(15), 2473–2488. https://doi.org/10.1175/1520-0469(1998)055%3C2473:IGWBIT%3E2.0.CO;2

Lelong, M.-P., & Dunkerton, T. J. (1998b). Inertia–gravity wave breaking in three dimensions. Part II: Convectively unstable waves. *Journal of the Atmospheric Sciences*, *55*(15), 2489–2501. https://doi.org/10.1175/1520-0469(1998)055%3C2489:IGWBIT%3E2.0.CO;2

Liu, H.-L., & Hagan, M. E. (1998). Local heating/cooling of the mesosphere due to gravity wave and tidal coupling. *Geophysical Research Letters*, *25*(15), 2941–2944. https://doi.org/10.1029/98GL02153

Liu, H.-L., Hagan, M. E., & Roble, R. G. (2000). Local mean state changes due to gravity wave breaking modulated by the diurnal tide. *Journal of Geophysical Research*, *105*(D10), 12,381–12,396. https://doi.org/10.1029/1999JD901163

Liu, H.-L., & Meriwether, J. W. (2004). Analysis of a temperature inversion event in the lower mesosphere. *Journal of Geophysical Research*, *109*, D02S07. https://doi.org/10.1029/2002JD003026

Lübken, F.-J. (1997). Seasonal variation of turbulent energy dissipation rates at high latitudes as determined by in situ measurements of neutral density fluctuations. *Journal of Geophysical Research*, *102*(D12), 13,441–13,456. https://doi.org/10.1029/97JD00853

Lübken, F.-J., Rapp, M., & Hoffmann, P. (2002). Neutral air turbulence and temperatures in the vicinity of polar mesosphere summer echoes, *Journal of Geophysical Research*, *107*(D15), 4273. https://doi.org/10.1029/2001JD000915

Luce, H., Crochet, M., Dalaudier, F., & Sidi, C. (1995). Interpretation of VHF ST radar vertical echoes from in situ temperature sheet observations. *Radio Science*, *30*, 1002–1025.

Luce, H., Crochet, M., Hanuise, C., Yamamoto, M., & Fukao, S. (1999). On the interpretation of the layered structures detected by MST radars in dual frequency domain interferometry (FDI) mode. *Radio Science*, *34*(5), 1077–1083. https://doi.org/10.1029/1999RS900045

Luce, H., Fukao, S., Dalaudier, F., & Crochet, M. (2002). Strong mixing events observed near the tropopause with the MU radar and high-resolution balloon techniques. *Journal of the Atmospheric Sciences*, *59*(20), 2885–2896. https://doi.org/10.1175/1520-0469(2002)059%3C2885:SMEONT%3E2.0.CO;2

Lund, T., & Fritts, D. C. (2012). Gravity wave breaking and turbulence generation in the thermosphere. *Journal of Geophysical Research*, *117*, D21105. https://doi.org/10.1029/JD017536

Luo, Z., & Fritts, D. C. (1993). Gravity wave excitation by geostrophic adjustment of the jet stream. Part II: Three-dimensional forcing. *Journal of the Atmospheric Sciences*, *50*(1), 104–115. https://doi.org/10.1175/1520-0469(1993)050%3C0104:GWEBGA%3E2.0.CO;2

McIntyre, M. E. (1989). On dynamics and transport near the polar mesopause in summer. *Journal of Geophysical Research*, *94*(D12), 14,617–14,628. https://doi.org/10.1029/JD094iD12p14617

Medvedev, A. S., & Klaassen, G. P. (1995). Vertical evolution of gravity wave spectra and the parameterization of associated wave drag. *Journal of Geophysical Research*, *100*(D12), 25,841–25,853. https://doi.org/10.1029/95JD02533

Meriwether, J. W., Dao, P. D., McNutt, R. T., Klemetti, W., Moskowitz, W., & Davidson, G. (1994). Rayleigh lidar observations of mesosphere temperature structure. *Journal of Geophysical Research*, *99*(D8), 16,973–16,987. https://doi.org/10.1029/94JD00666

Meriwether, J. W., Gao, X., Wickwar, V. B., Wilkerson, T., Beissner, K., Collins, S., & Hagan, M. E. (1998). Observed coupling of the mesosphere inversion layer to the thermal tidal structure. *Geophysical Research Letters*, *25*(9), 1479–1482. https://doi.org/10.1029/98GL00756

Meriwether, J. W., & Gerrard, A. J. (2004). Mesosphere inversion layers and stratosphere temperature enhancements. *Reviews of Geophysics*, *42*, RG3003. https://doi.org/10.1029/2003RG000133

Miller, A. D., Fritts, D. C., Chapman, D., Jones, G., Limon, M., Araujo, D., … Wang, L. (2015). Stratospheric imaging of noctilucent clouds: A new window on small-scale atmospheric dynamics. *Geophysical Research Letters*, *42*(14), 6058–6065. https://doi.org/10.1002/2015GL064758

Muschinski, A., & Wode, C. (1998). First in situ evidence for coexisting submeter temperature and humidity sheets in the lower free troposphere. *Journal of the Atmospheric Sciences*, *55*(18), 2893–2906. https://doi.org/10.1175/1520-0469(1998)055%3C2893:FISEFC%3E2.0.CO;2

Nappo, C. J. (2013). *An introduction to atmospheric gravity waves*. London: Academic Press.

Nastrom, G. D., & Eaton, F. D. (2001). Persistent layers of enhanced Cn2 in the lower stratosphere from radar. *Radio Science*, *36*(1), 137–149. https://doi.org/10.1029/2000RS002318

Oberheide, J., Liu, H.-L., Gusev, O. A., & Offermann, D. (2006). Mesospheric surf zone and temperature inversion layers in early November 1994. *Journal of Atmospheric and Solar - Terrestrial Physics*, *68*(15), 1752–1763. https://doi.org/10.1016/j.jastp.2005.11.013

Plougonven, R., & Zhang, F. (2014). Internal gravity waves from atmospheric jets and fronts. *Reviews of Geophysics*, *52*(1), 33–76. https://doi.org/10.1002/2012RG000419.

Rapp, M., Strelnikov, B., Müllemann, A., Lübken, F.-J., & Fritts, D. C. (2004). Turbulence measurements implications for gravity wave dissipation during the MaCWAVE/MIDAS summer rocket program. *Geophysical Research Letters*, *31*(24), L24S07. https://doi.org/10.1029/2003GL019325

Salby, M., Sassi, F., Callaghan, P., Wu, D., Keckhut, P., & Hauchecorne, A. (2002). Mesospheric inversions and their relationship to planetary wave structure. *Journal of Geophysical Research*, *107*(D4), 4041. https://doi.org/10.1029/2001JD000756

Sassi, F., Garcia, R. R., Boville, B. A., & Liu, H. (2002). On temperature inversions and the mesospheric surf zone. *Journal of Geophysical Research*, *107*(D19), 4380. https://doi.org/10.1029/2001JD001525

Schmidlin, F. J. (1976). Temperature inversions near 75 km. *Geophysical Research Letters*, *3*(3), 173–173, 176. https://doi.org/10.1029/GL003i003p00173

Schneider, A., Gerding, M., & Lübken, F.-J. (2015). Comparing turbulent parameters obtained from LITOS and radiosonde measurements. *Atmospheric Chemistry and Physics*, *15*(4), 2159–2166. https://doi.org/10.5194/acp-15-2159-2015

Schoeberl, M. R., Strobel, D. F., & Apruzese, J. P. (1983). A numerical model of gravity wave breaking and stress in the mesosphere. *Journal of Geophysical Research*, *88*(C9), 5249–5259. https://doi.org/10.1029/JC088iC09p05249

Strobel, D. F., Apruzese, J. P., & Schoeberl, M. R. (1985). Energy balance constraints on gravity wave induced eddy diffusion in the mesosphere and lower thermosphere. *Journal of Geophysical Research*, *90*(D7), 13,067–13,072. https://doi.org/10.1029/JD090iD07p13067

Strobel, D. F., Summers, M. E., Bevilacqua, R. M., DeLand, M. T., & Allen, M. (1987). Vertical constituent transport in the mesosphere. *Journal of Geophysical Research*, *92*(D6), 6691–6698. https://doi.org/10.1029/JD092iD06p06691

Sutherland, B. R. (2010). *Internal Gravity Waves*. Cambridge: Cambridge University Press. https://doi.org/10.1017/CBO9780511780318

Szewczyk, A., Strelnikov, B., Rapp, M., Strelnikova, I., Baumgarten, G., Kaifler, N., … Hoppe, U.-P. (2013). Simultaneous observations of a mesospheric inversion layer and turbulence during the ECOMA-2010 rocket campaign. *Annales Geophysicae*, *31*(5), 775–785. https://doi.org/10.5194/angeo-31-775-2013

Thomas, L., Marsh, A., Wareing, D., Astin, I., & Chandra, H. (1996). VHF echoes from the midlatitude mesosphere and the thermal structure observed by lidar. *Journal of Geophysical Research*, *101*(D8), 12,867–12,877. https://doi.org/10.1029/96JD00218

Thorpe, S. A. (1973a). Experiments on instability and turbulence in a stratified shear flow. *Journal of Fluid Mechanics*, *61*(04), 731–751. https://doi.org/10.1017/S0022112073000911

Thorpe, S. A. (1973b). Turbulence in stably stratified fluids: A review of laboratory experiments. *Boundary-Layer Meteorology*, *5*(95–119), 541–549.

Tsuda, T., VanZandt, T. E., Mizumoto, M., Kato, S., & Fukao, S. (1991). Spectral analysis of temperature and Brunt-Väisälä frequency fluctuations observed by radiosondes. *Journal of Geophysical Research*, *96*(D9), 17,265–17,278. https://doi.org/10.1029/91JD01944

Vadas, S. L., & Fritts, D. C. (2001). Gravity wave radiation and mean responses to local body forces in the atmosphere. *Journal of the Atmospheric Sciences*, *58*(16), 2249–2279. https://doi.org/10.1175/1520-0469(2001)058%3C2249:GWRAMR%3E2.0.CO;2

Vanneste, J. (1995). The instability of internal gravity waves to localized disturbances. *Annales Geophysicae*, *13*(2), 196–210. https://doi.org/10.1007/s00585-995-0196-7

VanZandt, T. E., & Fritts, D. C. (1989). A theory of enhanced saturation of the gravity wave spectrum due to increases in atmospheric stability. *Pure and Applied Geophysics*, *130*(2-3), 399–420. https://doi.org/10.1007/BF00874466

von Zahn, U., & Meyer, W. (1989). Mesopause temperatures in polar summer. *Journal of Geophysical Research*, *94*(D12), 14,647–14,651. https://doi.org/10.1029/JD094iD12p14647

Walterscheid, R. L. (2000). Propagation of small-scale gravity waves through large-scale internal wave fields: Eikonal effects at low-frequency approximation critical levels. *Journal of Geophysical Research*, *105*(D14), 18,027–18,037. https://doi.org/10.1029/2000JD900207

Walterscheid, R. L., & Schubert, G. (1990). Nonlinear evolution of an upward propagating gravity wave: Overturning, convection, transience and turbulence. *Journal of the Atmospheric Sciences*, *47*(1), 101–125. https://doi.org/10.1175/1520-0469(1990)047%3C0101:NEOAUP%3E2.0.CO;2

Wang, L., Fritts, D. C., Williams, B. P., Goldberg, R. A., Schmidlin, F. J., & Blum, U. (2006). Gravity waves in the middle atmosphere during the MaCWAVE winter campaign. *Annales de Geophysique*, *24*(4), 1209–1226. https://doi.org/10.5194/angeo-24-1209-2006

Warner, C. D., & McIntyre, M. E. (2001). An ultra-simple spectral parameterization for non-orographic gravity waves. *Journal of the Atmospheric Sciences*, *58*(14), 1837–1857. https://doi.org/10.1175/1520-0469(2001)058%3C1837:AUSPFN%3E2.0.CO;2

Werne, J., & Fritts, D. C. (1999). Stratified shear turbulence: Evolution and statistics. *Geophysical Research Letters*, *26*(4), 439–442. https://doi.org/10.1029/1999GL900022

Whiteway, J., Carswell, A. I., & Ward, W. E. (1995). Mesospheric temperature inversions with overlaying nearly adiabatic lapse rate: An indication of well-mixed turbulent layer. *Geophysical Research Letters*, *22*(10), 1201–1204. https://doi.org/10.1029/95GL01109

Whiteway, J. A., Pavelin, E. G., Busen, R., Hacker, J., & Vosper, S. (2003). Airborne measurements of gravity wave breaking at the tropopause. *Geophysical Research Letters*, *30*(20), 2070. https://doi.org/10.1029/2003GL018207

Williams, B. P., Fritts, D. C., She, C. Y., Baumgarten, G., & Goldberg, R. A. (2006). Gravity wave propagation, tidal interaction, and instabilities in the mesosphere and lower during the winter 2003 MaCWAVE rocket campaign, MaCWAVE special issue of. *Annales Geophysicae*, *24*(4), 1199–1208. https://doi.org/10.5194/angeo-24-1199-2006

Williams, B. P., White, M. A., Krueger, D. A., & She, C. Y. (2002). Observation of a large amplitude wave and inversion layer leading to convective instability in the mesopause over Fort Collins, CO (413N, 1053W). *Geophysical Research Letters*, *29*(17), 1850. https://doi.org/10.1029/2001GL014514

Woodman, R. F., Michhue, G., Röttger, J., & Castillo, O. (2007). The SOUSY radar at Jicamarca: High altitude-resolution capabilities, MST-11 Workshop, Gadanki (pp. 4).

Wu, D. (2000). Mesospheric temperature inversion layers: Recent observations from UARS ISAMS and MLS. *Recent Research Developments in Geophysics*, *3*, 37–44.

Yiğit, E., Aylward, A. D., & Medvedev, A. S. (2008). Parameterization of the effects of vertically propagating gravity waves for thermosphere general circulation models: Sensitivity study. *Journal of Geophysical Research*, *113*, D19106. https://doi.org/10.1029/2008JD010135

Yiğit, E., & Medvedev, A. S. (2015). Internal wave coupling processes in Earth's atmosphere. *Advances in Space Research*, *55*(4), 983–1003. https://doi.org/10.1016/j.asr.2014.11.020